Elevated glycolytic metabolism of monocytes limits the generation of HIF-1α-driven migratory dendritic cells in tuberculosis

Mariano Maio[1,2], Joaquina Barros[1,2], Marine Joly[2,3], Zoi Vahlas[2,3], , José Luis Marín Franco[1,2], Melanie Genoula[1,2], Sarah Monard[2,3], María Belén Vecchione[4], Federico Fuentes[1], Virginia Gonzalez Polo[4], María Florencia Quiroga[4], Mónica Vermeulen[1], Thien-Phong Vu Manh[5], Rafael J Argüello[5], Sandra Inwentarz[6], Rosa Musella[6], Lorena Ciallella[6], Pablo González Montaner[6], Domingo Palmero[6], Geanncarlo Lugo Villarino[2,3], María del Carmen Sasiain[1,2], Olivier Neyrolles[2,3], Christel Verollet[2,3,#], and Luciana Balboa[1,2,4,#,*]

[1] Instituto de Medicina Experimental (IMEX)-CONICET, Academia Nacional de Medicina, Buenos Aires, Argentina.

[2] International Associated Laboratory (LIA) CNRS IM-TB/HIV (1167), Buenos Aires, Argentina / International Research Project Toulouse, France

[3] Institut de Pharmacologie et de Biologie Structurale, Université de Toulouse, CNRS, UPS, Toulouse, France

[4] Consejo Nacional de Investigaciones Científicas y Técnicas (CONICET)-Universidad de Buenos Aires. Instituto de Investigaciones Biomédicas en Retrovirus y Sida (INBIRS), Buenos Aires, Argentina

[5] Aix Marseille University, CNRS, INSERM, CIML, Centre d'Immunologie de Marseille-Luminy, Marseille, France

[6] Instituto Prof. Dr. Raúl Vaccarezza and Hospital de Infecciosas Dr. F.J. Muñiz, Buenos Aires, Argentina

[#] These senior authors contributed equally to this work

* **Corresponding Author**: Luciana Balboa, Paraguay 2155, Piso 11 CABA (C1121ABG), Argentina. + 54(011) 4508-3689, luciana_balboa@hotmail.com

"The authors have declared that no conflict of interest exists."

Abstract

During tuberculosis, migration of dendritic cells (DCs) from the site of infection to the draining lymph nodes is known to be impaired, hindering the rapid development of protective T-cell mediated immunity. However, the mechanisms involved in the delayed migration of DCs during tuberculosis (TB) are still poorly defined. Here, we found that infection of DCs with *Mycobacterium tuberculosis* (Mtb) triggers HIF-1α-mediated aerobic glycolysis in a TLR2-dependent manner, and that this metabolic profile is essential for DC migration. In particular, the lactate dehydrogenase (LDH) inhibitor oxamate and the HIF-1α inhibitor PX-478 abrogated Mtb-induced DC migration *in vitro* to the lymphoid tissue-specific chemokine CCL21, and *in vivo* to lymph nodes in mice. Strikingly, we found that although monocytes from TB patients are inherently biased toward glycolysis metabolism, they differentiate into poorly glycolytic and poorly migratory DCs, compared with healthy subjects. Taken together, these data suggest that because of their preexisting glycolytic state, circulating monocytes from TB patients are refractory to differentiation into migratory DCs, which may explain the delayed migration of these cells during the disease and opens avenues for host-directed therapies for TB.

54 **Graphical Abstract**

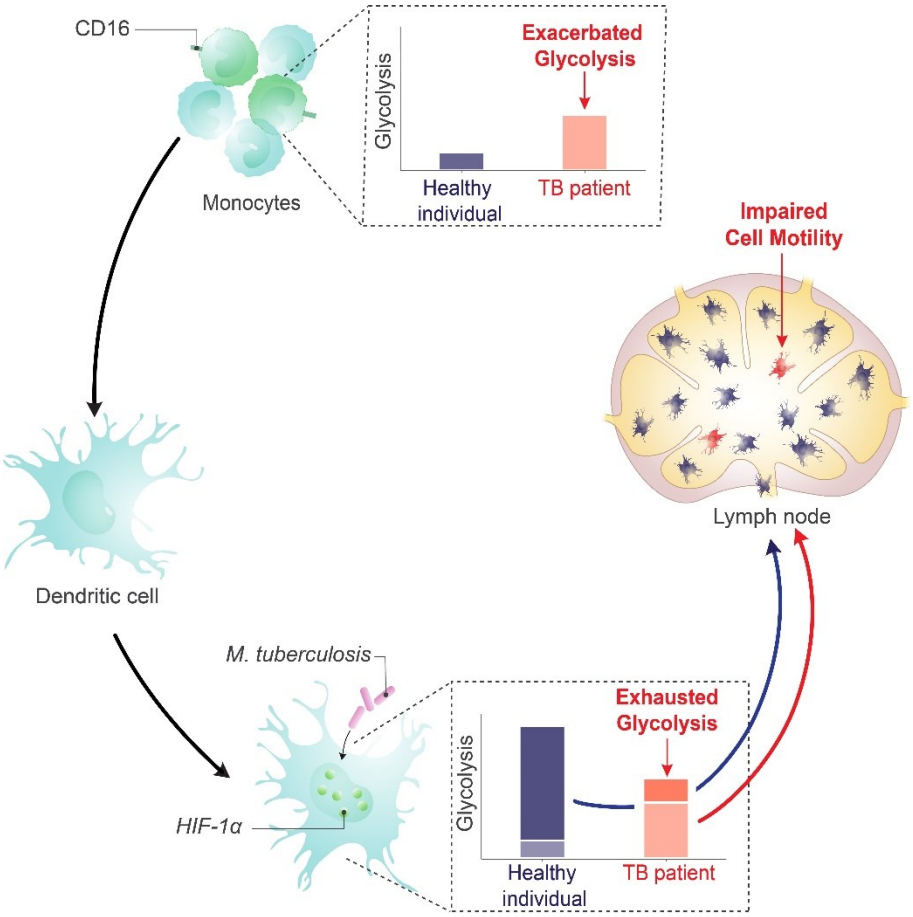

55

56

57

Introduction

Tuberculosis (TB) remains a major global health problem, responsible for approximately 1.6 million deaths annually. The causative agent of TB, *Mycobacterium tuberculosis* (Mtb), is a highly successful pathogen that has evolved several strategies to weaken the host immune response. Although reliable immune correlates of protective immunity against Mtb are still not well-defined, it is widely accepted that Th1 cells contribute to protection by secreting IFN-γ and promoting antimycobacterial activity in macrophages[1]. Importantly, the induction of a strong Th1 immune response relies on the generation of immunogenic dendritic cells (DCs) with strong migratory properties[2–5]. Mtb has been shown to interfere with several DC functions, thus impairing the induction and development of adaptive immunity[6–8]. For instance, we and others previously reported that Mtb-exposed DCs have low capacity for mycobacterial antigen presentation and stimulation of Mtb-specific $CD4^+$ T cells[9–13]. Additionally, Mtb-infected DCs were reported to have an impaired ability to migrate to lymph nodes *in vitro*[14,15] and *in vivo* in murine models[3,5]; however, the underlying molecular mechanisms of these phenotypes and their relevance to the migratory activity of monocyte-derived DCs in TB patients remain unknown.

Rapid, directed migration of DCs towards secondary lymphoid organs requires essential changes at the cellular and molecular levels[16]. Relatedly, the metabolic state of DCs is complex and varies according to cell origin, differentiation and maturation states, as well as local microenvironment, among other factors[17–20]. Studies have reported that upon pathogen sensing, the transcription factor hypoxia-inducible factor-1α (HIF-1α) increases glycolysis, which promotes immunogenic functions of DCs, such as IL-12 production, costimulatory marker expression[21], and cell migration[22–24]. By contrast, it was shown that HIF-1α represses the proinflammatory output of LPS-stimulated DCs and can inhibit DC-induced T-cell responses in other settings[25]. To reconcile these disparate roles for HIF-1α, it has been proposed that the impact of metabolic pathway activation on DC

85 functions varies among DC subsets[18]. To this point, most prior studies have been
86 conducted using murine conventional DCs and plasmacytoid DCs[19]. Recently, with the
87 implementation of high-dimensional techniques, it was demonstrated that distinct
88 metabolic wiring is associated with individual differentiation and maturation stages of
89 DCs[26], highlighting the importance of defining the metabolic profile of specific subsets of
90 DCs under physiological or pathological conditions[20]. Given the key role of DCs in the
91 host response to TB, it is thus crucial to investigate DC metabolism in the context of Mtb
92 infection[27].

93 We previously demonstrated that the TB-associated microenvironment, as conferred by
94 the acellular fraction of TB patient pleural effusions, inhibits HIF-1α activity leading to a
95 reduction in glycolytic and microbicidal phenotypes in macrophages[28]. Moreover,
96 activation of HIF-1α enhances Mtb control at early times post-infection in mouse
97 models[29], and this effect was associated with a metabolic switch of alveolar
98 macrophages towards an M1-like profile[28]. Given that HIF-1α activation promotes
99 protection at early stages of Mtb infection and given its role as a key regulator of DC
100 migration and inflammation[30], we hypothesized that HIF-1α could affect the functionality
101 of DCs in regulating the initiation and orchestration of the adaptive immune response to
102 Mtb, a process known to be delayed upon Mtb infection[5,6]. Here, we show that HIF-1α-
103 mediated glycolysis promotes DC activation and migration in the context of TB.
104 Importantly, we report active glycolysis in monocytes from TB patients, which leads to
105 poor glycolytic induction and migratory capacities of monocyte-derived DCs.

106 **Results**

107 **Mtb impacts metabolism in human monocyte-derived DCs**

108 To determine the impact of Mtb on the metabolism of human monocyte-derived DCs
109 (Mo-DCs), we assessed metabolic parameters associated with glycolysis and
110 mitochondrial changes upon Mtb stimulation or infection. Cells undergoing aerobic
111 glycolysis are characterized by increased consumption of glucose and the production
112 and release of lactate. We measured lactate release and glucose consumption in Mo-
113 DCs stimulated for 24 h with equivalent doses of either irradiated (iMtb) or viable Mtb.
114 DCs treated with either iMtb or viable Mtb released increased levels of lactate and
115 consumed more glucose than untreated DCs (**Figure 1A-B**). Consistently, both iMtb
116 treatment and Mtb infection resulted in an increase in expression of the key glycolysis-
117 activating regulator HIF-1α at both mRNA and protein levels (**Figure 1C-D**). Expression
118 of the gene encoding the glycolytic enzyme lactate dehydrogenase A (*LDHA*), which
119 catalyzes the conversion of lactate to pyruvate, was also increased in iMtb-treated or
120 Mtb-infected DCs (**Figure 1E**). In agreement with their enhanced glycolysis profile, DCs
121 stimulated with iMtb or infected with viable Mtb had increased expression of the glucose
122 transporter GLUT1 (SLC2A1)[31] (**Figure 1F)**. Of note, *LDHA* and *GLUT1* are HIF-1α
123 target genes, and their upregulation correlated with the increase in HIF-1α expression
124 upon Mtb stimulation. To assess changes in the mitochondria, we measured
125 mitochondrial mass and morphology. We found a higher mitochondrial mass as well as
126 larger individual mitochondria in iMtb-stimulated DCs compared to untreated DCs
127 (**Figure 1G-H**). In contrast to the findings obtained upon iMtb stimulation, Mtb-infected
128 DCs displayed a reduction in their mitochondrial mass (**Figure 1G**). This result indicates
129 that although both Mtb-infected and irradiated Mtb-exposed DCs show a clear increase
130 in their glycolytic activity, divergent responses are observed in terms of mitochondrial
131 mass. Therefore, our data indicate that Mtb impacts the metabolism of Mo-DCs, leading
132 to mitochondrial changes and triggering glycolysis-associated parameters.

133

134 **Mtb exposure shifts DCs to a glycolytic profile over oxidative phosphorylation**

135 To further characterize the metabolic profile of DCs upon iMtb-stimulation or Mtb-
136 infection, we next evaluated the metabolism of DCs at single-cell level using the
137 SCENITH technology[32]. This method is based on a decrease in ATP levels that is tightly
138 coupled with a decrease in protein synthesis and displays similar kinetics[32]. By treating
139 the cells with glucose or mitochondrial respiration inhibitors, and measuring their impact
140 on protein synthesis by puromycin incorporation via flow cytometry, glucose and
141 mitochondrial dependences can be quantified. Two additional derived parameters such
142 as “glycolytic capacity” and “fatty acid and amino acid oxidation (FAO & AAO) capacity”
143 were also calculated. SCENITH technology revealed a lower reliance on oxidative
144 phosphorylation (OXPHOS) in parallel with an increase in the glycolytic capacity of iMtb-
145 stimulated (**Figure 2A-B),** Mtb-infected DCs and even bystander DCs (those cells that
146 are not directly infected but stand nearby) (**Figure 2C-D**). Since bystander DCs are not
147 in direct association with Mtb (Mtb-RFP- DCs), soluble mediators induced in response
148 to infection may be sufficient to trigger glycolysis even in uninfected cells. No differences
149 were observed for glucose dependence and FAO & AAO capacity (**Figure 2A-D**).
150 Additionally, we found no changes between the FAO dependency in Mtb-stimulated DCs
151 in comparison to control cells when the FAO inhibitor (etomoxir) was used (**Figure S1A**).
152 For the case of iMtb-stimulated DCs, we also assessed the intracellular rates of glycolytic
153 and mitochondrial ATP production using Seahorse technology. Bioenergetic profiles
154 revealed that iMtb increased the rate of protons extruded over time, or proton efflux rate
155 (PER), as well as the basal oxygen consumption rate (OCR) in Mo-DCs (**Figure 2E**).
156 The measurements of basal extracellular acidification rate (ECAR) and OCR were used
157 to calculate ATP production rate from glycolysis (GlycoATP) and mitochondrial OXPHOS
158 (MitoATP). The ATP production rates from both glycolysis and mitochondrial respiration
159 were augmented upon iMtb-stimulation (**Figure 2F**). Similar to SCENITH results, the
160 relative contribution of GlycoATP to overall ATP production was increased, while

161 MitoATP contribution was decreased in iMtb-treated cells compared to untreated cells
162 (**Figure 2G**). These results confirmed the change in DC metabolism induced by Mtb,
163 with an increase in the relative glycolytic contribution to overall metabolism at the
164 expense of the OXPHOS pathway. Together, metabolic profiling indicates that a
165 metabolic switch toward aerobic glycolysis occurs in Mo-DCs exposed to Mtb.
166

167 **Mtb triggers the glycolytic pathway through TLR2 ligation**

168 Since Mtb is sensed by Toll-like receptors (TLR)-2 and -4[33], we investigated the
169 contribution of these receptors to glycolysis activation in Mo-DCs upon Mtb stimulation.
170 Using specific neutralizing antibodies for these receptors, we found that TLR2 ligation,
171 but not that of TLR4, was required to trigger the glycolytic pathway, as reflected by a
172 decrease in lactate release, glucose consumption and HIF-1α expression in iMtb-
173 stimulated DCs treated with an anti-TLR2 antibody (**Figure 3A-C**). As a control, and as
174 expected given the reliance on TLR4 for LPS sensing[34], lactate release and glucose
175 consumption were abolished in LPS-stimulated DCs in the presence of neutralizing
176 antibodies against TLR4 but not TLR2 (**Figure S2A-B**). Moreover, blockade of TLR2
177 also diminished glycolytic ATP production in iMtb-stimulated DCs without altering
178 OXPHOS-associated ATP production (**Figure 3D**) or the size and morphology of
179 mitochondria (**Figure S2C**), suggesting that TLR2 engagement by iMtb is required for
180 the induction of glycolysis but not mitochondrial respiration. Interestingly, TLR2 ligation
181 was also necessary for lactate release and HIF-1α up-regulation triggered by viable Mtb,
182 (**Figure S2D-E**). To further confirm the involvement of TLR2 in the induction of glycolysis,
183 we tested the effect of synthetic (Pam_3CSK_4) or mycobacterial (peptidoglycans, PTG)
184 TLR2 agonists[35,36] and found that both ligands induced lactate release and glucose
185 consumption in DCs (**Figure 3E-F**), without affecting cell viability (**Figure S2F**). Thus,
186 our data indicate that Mtb induces glycolysis in Mo-DCs through TLR2 engagement.
187

188 **HIF-1α is required for DC maturation upon iMtb stimulation but not for CD4⁺ T**
189 **lymphocyte polarization**

190 To determine the impact of glycolysis on DC maturation and the capacity to activate T
191 cells, we inhibited HIF-1α activity in iMtb-stimulated DCs employing two HIF-1α inhibitors
192 that display different mechanisms of action. The first is PX-478 (PX) that lowers HIF-1α
193 levels by inhibiting HIF-1α deubiquitination, decreases HIF-1α mRNA expression, and
194 reduces HIF-1α translation[37]; the second one is echinomycin (Ech), which inhibits the
195 binding of HIF-1α to the hypoxia response element thereby blocking HIF-1α DNA binding
196 capability[38,39]. Treatment with either HIF-1α inhibitor PX or Ech diminished lactate release
197 and glucose consumption in iMtb-stimulated DCs without affecting cell viability at the
198 indicated concentration (**Figure S3A-F**). HIF-1α inhibition by PX significantly abolished
199 ATP production associated with glycolysis without affecting absolute levels of OXPHOS-
200 derived ATP production in iMtb-stimulated DCs (**Figure 4A and Figure S3G**). In line with
201 these results, the glycolytic capacity was reduced in iMtb-stimulated DCs treated with
202 Ech (**Figure S3H**). Although HIF-1α inhibitors did not affect the uptake of iMtb by DCs
203 (**Figure S3I**), we observed a reduction in the expression of activation markers CD83 and
204 CD86, but not in the inhibitory molecule PD-L1, upon treatment with PX (**Figure 4B**) or
205 Ech (**Figure S4**)**.** We then measured cytokine production in iMtb-stimulated DCs after
206 HIF-1α inhibition and noted a reduction in TNF-α and an increase in IL-10 production by
207 PX-treated cells (**Figure 4C**). To assess the capacity of DCs to activate T cells in
208 response to mycobacterial antigens, we co-cultured DCs and autologous CD4⁺ T cells
209 from PPD⁺ donors in the presence or absence of HIF-1α inhibitors and measured the
210 overall IFN-γ and IL-17 production in culture supernatants as well as cell surface
211 expression of T cell markers. We found no significant differences in the activation profile
212 of autologous CD4⁺ T cells in coculture with iMtb-stimulated DCs treated or not with PX
213 (**Figure 4D-E and Figure S5**). We conclude that while HIF-1α is important for the
214 maturation of iMtb-stimulated Mo-DCs, it does not influence their capacity to activate
215 CD4⁺ T cells, at least *in vitro*.

216

217 **HIF-1α-mediated glycolysis triggers the motility of DCs upon iMtb stimulation**

218 Since DC migration to lymph nodes is essential to initiate an adaptive immune response
219 and glycolytic activity has been reported to control DC migration upon stimulation[22,23], we
220 evaluated the migratory properties of iMtb-stimulated DCs in the presence of inhibitors
221 of HIF-1α and LDH which catalyzes the interconversion of pyruvate and lactate. First, we
222 confirmed that PX and oxamate (OX), a well-established LDH inhibitor, diminished the
223 glycolytic activity of iMtb-stimulated human Mo-DCs, as demonstrated by reduced lactate
224 release (**Figure S3A and 5A**). Next, using a transwell migration assay, we found that
225 PX and OX treatment significantly diminished the chemotactic activity of iMtb-stimulated
226 human Mo-DCs in response to CCL21 (**Figure 5B**), a CCR7 ligand responsible for the
227 migration of DCs into lymphoid organs. We also assessed the 3 dimensional (3D)
228 migration capacity of iMtb-stimulated DCs through a collagen matrix in which DCs use
229 an amoeboid migration mode[40] and found that 3D migration was significantly impaired
230 upon HIF-1α or glycolysis inhibition (**Figure 5C**). The role of glycolysis in the migration
231 of iMtb-stimulated Mo-DCs was further confirmed using an additional LDHA inhibitor,
232 GSK2837808A, which reduced both the release of lactate by iMtb-stimulated Mo-DCs
233 and their migration in response to CCL21 (**Figure S6A-B**). Attenuation of cell migration
234 through collagen induced by OX and PX was also confirmed in Mtb-infected DCs (**Figure
235 5D**). To further investigate the effects of glycolysis on cell migration, we turned to an *in
236 vivo* model. Murine bone marrow-derived DCs (BMDCs) isolated and stimulated with
237 iMtb in the presence or absence of PX or OX were labeled with CFSE and transferred
238 into naïve mice (**Figure 5E**). Similar to human Mo-DCs, iMtb stimulation increased
239 glycolysis in BMDCs, which was inhibited by PX and OX treatment *in vitro* (**Figure S6C**).
240 Three hours after the transfer of BMDCs into recipient mice, nearby lymph nodes were
241 collected for DC quantification (**Figure 5E**). A higher number of adoptively transferred
242 DCs (CFSE-labeled $CD11c^+$ cells) were detected in lymph nodes from mice that received
243 iMtb-stimulated BMDCs compared to mice that received untreated BMDCs or iMtb-

244 BMDCs treated with either PX or OX (**Figure 5F and Figure S6D**). Of note, we verified
245 that CCR7 expression on iMtb-stimulated BMDCs was not affected by OX or PX
246 treatment, so the effect could not be ascribed to downregulation of the chemokine
247 receptor (**Figure S6E**). Therefore, we conclude that HIF-1α-mediated glycolysis is
248 required for the successful migration of iMtb-stimulated DCs into lymph nodes.
249

250 **Stabilization of HIF-1α promotes migration of tolerogenic DCs and DCs derived**
251 **from TB patient monocytes**

252 Since DC differentiation is skewed, at least partially, towards a tolerogenic phenotype
253 during TB[41–43], we investigated whether tolerogenic DCs can be reprogrammed into
254 immunogenic DCs by modulating their glycolytic pathway after iMtb stimulation. To this
255 end, we generated tolerogenic Mo-DCs by adding dexamethasone (Dx) before
256 stimulation with iMtb in the presence or absence of dimethyloxalylglycine (DMOG), which
257 stabilizes the expression of HIF-1α. HIF-1α expression is tightly regulated by prolyl
258 hydroxylase domain containing proteins which facilitate the recruitment of the von
259 Hippel-Lindau (VHL) protein, leading to ubiquitination and degradation of HIF-1α by the
260 proteasomes[44]. DMOG inhibits the prolyl hydroxylase domain-containing proteins.
261 Acquisition of the tolerogenic phenotype was confirmed by the lack of upregulation of
262 costimulatory markers CD83 and CD86, as well as by increased PD-L1 expression in
263 iMtb-DCs treated with Dx compared to control iMtb-DCs (**Figure S7A**). Moreover, Dx-
264 treated DCs did not exhibit an increase in lactate release, consumption of glucose or
265 induction of HIF-1α expression in response to iMtb, showing a high consumption of levels
266 of glucose under basal conditions (**Figure 6A-B**). Of note, HIF-1α stabilization using
267 DMOG restored the HIF-1α expression and lactate production in response to iMtb in Dx-
268 treated DCs and increased the consumption of glucose (**Figure 6A-B**). Activation of HIF-
269 1α also improved 3D amoeboid migration, as well as 2D migration capacity of DCs
270 towards CCL21 of iMtb-stimulated Dx-treated DCs (**Figure 6C-D and Figure S7B**).
271 Confirming the relevance of these findings to human TB patients, we found that iMtb-

272 stimulated Mo-DCs from TB patients were deficient in their capacity to migrate towards
273 CCL21 (**Figure 6E**) and in glycolytic activity, compared to Mo-DCs from healthy subjects
274 (**Figure 6F-G**). Strikingly, stabilizing HIF-1α expression using DMOG in Mo-DCs from
275 TB patients restored their chemotactic activity in response to iMtb (**Figure 6H**). These
276 data indicate that the impaired migratory capacity of iMtb-stimulated tolerogenic DCs or
277 TB patient-derived DCs can be restored via HIF-1α stabilization; thus, glycolysis is critical
278 for DC function during TB in both murine and human contexts.
279

280 **CD16^{+} monocytes from TB patients show increased glycolytic capacity**

281 Since we observed differences in the metabolic activity of DCs derived from monocytes
282 of TB patients when compared to healthy donors, we next focused on evaluating the
283 release of lactate by DC precursors from both subject groups during the first hours of DC
284 differentiation with IL-4/GM-CSF. We found a high release of lactate by monocytes from
285 TB patients compared to healthy donors after 1 h of differentiation (**Figure 7A**). Lactate
286 accumulation increased in both subject groups after 24 h with IL-4/GM-CSF (**Figure 7A**).
287 Based on these differential glycolytic activities displayed by DC precursors from both
288 subject groups at very early stages of the differentiation process, we decided to evaluate
289 the *ex vivo* metabolic profile of monocytes using SCENITH. To this end, we assessed
290 the baseline glycolytic capacity of the three main populations of monocytes: classical
291 (CD14^{+}CD16^{-}), intermediate (CD14^{+}CD16^{+}), and non-classical (CD14^{dim}CD16^{+})
292 monocytes. We found that both populations of CD16^{+} monocytes from TB patients had
293 a higher glycolytic capacity than monocytes from healthy donors (**Figure 7B**). Moreover,
294 the glycolytic capacity of CD16^{+} monocytes (CD14^{+}CD16^{+} and CD14^{dim}CD16^{+})
295 correlates with time since the onset of TB-related symptoms (**Figure 7C**), with no
296 association to the extent or severity of lung disease (unilateral/bilateral lesions and
297 with/without cavities, **Figure S8**). To further expand the metabolic characterisation of
298 monocyte subsets from TB patients, we used previously published transcriptomic data
299 (GEO accession number: GSE185372) of CD14^{+}CD16^{-}, CD14^{+}CD16^{+} and

300 $CD14^{dim}CD16^{+}$ monocytes isolated from individuals with active TB, latent TB ($IGRA^{+}$), as
301 well as from TB negative healthy controls ($IGRA^{-}$)[45]. Within this framework, we performed
302 high-throughput GeneSet Enrichment Analysis (GSEA) using the BubbleMap module of
303 BubbleGUM, which includes a multiple testing correction step to allow comparisons
304 between the three monocyte subsets[46]. As expected, this approach reveals enrichments
305 in genes associated with interferon responses (alpha and gamma) in patients with active
306 TB compared to healthy donors (either $IGRA^{-}$ or latent TB) for all three monocyte subsets
307 (**Figure 7D**). Consistent with our findings, glycolysis increases in active TB in both
308 $CD14^{+}CD16^{+}$ and $CD14^{dim}CD16^{+}$ monocytes (albeit not significant), while it appears to
309 decrease in classical $CD14^{+}CD16^{-}$ monocytes (**Figure 7D**). Unlike $CD14^{+}CD16^{-}$ cells,
310 the inflammatory response is notably enriched in $CD14^{+}CD16^{+}$ and $CD14^{dim}CD16^{+}$
311 monocytes from patients with active TB compared those with latent TB or healthy
312 subjects (**Figure 7D**), suggesting that their glycolytic profile correlates with a higher
313 inflammatory state. Finally, no significant enrichment of oxidative phosphorylation-
314 associated genes was found in any of the performed comparisons (**Figure 7D**). Taken
315 together, these results demonstrate that TB disease is associated with an increased
316 activation and glycolytic profile of circulating $CD16^{+}$ monocytes.
317

318 **HIF1-α activation in $CD16^{+}$ monocytes from TB patients leads to differentiated DCs**
319 **with a poor migration capacity**

320 Since circulating $CD16^{+}$ monocytes from TB patients are highly glycolytic, we evaluated
321 the expression of HIF1-α among the populations. We found that $CD16^{+}$ monocytes from
322 TB patients exhibited a higher expression of HIF1-α than from healthy donors (**Figure**
323 **8A**). As we have previously demonstrated that $CD16^{+}$ monocytes from TB patients
324 generate aberrant DCs[41], we hypothesized that the different metabolic profile of this
325 monocyte subset could yield DCs with some sort of exhausted glycolytic capacity and
326 thus lower migration activity upon Mtb exposure. To test this hypothesis, we treated with

327 DMOG to increase the activity of HIF-1α during the first 24 h of monocyte differentiation
328 from healthy donors, leading to an exacerbated increase in lactate release at early
329 stages of the differentiation (**Figure 8B**). Such early addition of DMOG to healthy
330 monocytes resulted in the generation of DCs (6 days with IL-4/GM-CSF) characterized
331 by equivalent levels of CD1a as control DCs, with a significant decrease in the
332 expression of DC-SIGN (**Figure S9A**). In terms of activation marker expression, DCs
333 differentiated from DMOG-pretreated cells responded to iMtb by upregulating CD86 at
334 higher levels compared to control cells, with an accompanying trend towards reduced
335 upregulation of CD83 (**Figure S9B**). We also observed that DCs from DMOG pretreated-
336 cells exhibited a lower migratory capacity in response to iMtb (**Figure 8C**), reminiscent
337 of the 2D migration capacities of Mo-DCs from TB patients. Altogether, our data suggest
338 that the activated glycolytic status of monocytes from TB patients leads to the generation
339 of DCs with low motility in response to Mtb.
340
341

342 **Discussion**

343 In this study, we provide evidence for the role of HIF-1α-mediated glycolysis in promoting
344 the migratory capacity of DCs upon encounter with iMtb. Our approach to quantify the
345 *ex vivo* metabolism of monocytes shows that CD16$^+$ monocytes from TB patients display
346 an exacerbated glycolytic activity that may result in the generation of DCs with poor
347 migratory capacities in response to iMtb. Our results suggest that under extensive
348 chronic inflammatory conditions, such as those found in TB patients, circulating
349 monocytes may be metabolically preconditioned to differentiate into DCs with low
350 migratory potential.

351

352 Upon Mtb infection of naive mice, initial accumulation of activated CD4$^+$ T cells in the
353 lung is delayed, occurring between 2-3 weeks post-infection[3,47]. The absence of
354 sterilizing immunity induced by TB vaccines, such as BCG, has been proposed to result
355 from delayed activation of DCs and the resulting delay in antigen presentation and
356 activation of vaccine-induced CD4$^+$ T-cell responses[48]. In this context, it was
357 demonstrated that Mtb-infected Mo-DCs recruited to the site of infection exhibit low
358 CCR7 expression and impaired migration to lymph nodes compared to uninfected Mo-
359 DCs[49]. Additionally, Mo-DCs have been found to play a key role in transporting Mtb
360 antigens from the lung to the draining lymph node, where conventional DCs present
361 antigens to naive T cells[50]. The migratory capacity of responding DCs is thus of
362 paramount importance to the host response to Mtb infection.

363

364 Here, we found that Mtb exposure triggers glycolysis in Mo-DCs from healthy donors,
365 which promotes their migration capacity in a HIF-1α-dependent manner. Recently, it was
366 shown that glycolysis was required for CCR7-triggered murine DC migration in response
367 to LPS[22–24]. Glycolysis was also reported to be required for the migration of other immune
368 cells such as macrophages[51] and regulatory T cells[52]. Consistently, we show that

369 inhibition of HIF-1α-dependent glycolysis impairs human Mo-DC migration upon Mtb
370 stimulation. The link between cellular metabolism and migratory behavior are supported
371 by studies that have elucidated how glycolysis can be mechanically regulated by
372 changes in the architecture of the cytoskeleton, ultimately impacting the activity of
373 glycolytic enzymes[53,54]. In addition, interesting links between cellular mechanics and
374 metabolism have been previously described for DCs, highlighting the potential to alter
375 DC mechanics to control DC trafficking and consequently T cell priming[16]. However,
376 studies focused on the molecular mechanisms by which metabolic pathways impact the
377 machinery responsible for cell movement in the context of TB infection will be required
378 to better understand and design therapeutic manipulation.
379
380 Our research indicates that DCs exhibit upregulated glycolysis following stimulation or
381 infection by Mtb. This metabolic shift is crucial for facilitating cell migration to the draining
382 lymph nodes, an essential step in mounting an effective immune response. Yet, it
383 remains uncertain whether this glycolytic induction reaches a threshold conducive to
384 generating a protective immune response, a matter that our findings do not definitively
385 address. In addition, we demonstrated that tolerogenic DCs induced by dexamethasone
386 as well as DCs derived from TB patient monocytes exhibit lower lactate release and
387 impaired trafficking toward CCL21 upon Mtb stimulation; both phenotypes could be
388 rescued by stabilization of HIF-1α expression. To our knowledge, this is the first study to
389 address how the metabolic status of monocytes from TB patients influences the
390 migratory activity of further differentiated DCs. According to our findings, the activation
391 status of the glycolysis/HIF-1α axis in monocytes would be a predictor of refractoriness
392 to differentiation into migratory DCs in TB. With respect to the metabolism of tolerogenic
393 DCs broadly, our results are consistent with reported data showing that DC tolerance
394 can be induced by drugs promoting OXPHOS, such as vitamin D and dexamethasone[55–
395 57]. It was interesting to note that, although migration of tolerogenic DCs did not increase

396 upon Mtb stimulation, it was increased under basal conditions, which agrees with
397 previous data showing a high steady-state migration capacity of putatively tolerogenic
398 DCs[58].
399
400 It has been widely demonstrated that immune cells can switch to glycolysis following
401 engagement of TLRs[59]. Our work showed that TLR2 ligation by either viable or irradiated
402 Mtb was necessary to trigger glycolysis in DCs, at least at early times post-stimulation.
403 In fact, even bystander DCs increased their glycolytic activity in Mtb-infected cultures,
404 suggesting that mycobacterial antigens or bacterial debris present in the
405 microenvironment may be sufficient to trigger TLR-dependent glycolysis. In the context
406 of natural infection *in vivo*, we foresee that DC with different levels of infection will coexist,
407 some with low bacillary load that, according to our data, may be able to trigger glycolysis
408 and migrate, while others highly infected DCs would more likely die[60]. It remains to be
409 elucidated whether persistent interaction between DCs and Mtb might lead to an
410 attenuation in glycolysis over time, as has been reported for macrophages[61]. In this
411 regard, our data demonstrates that chronic Mtb infection leads to monocytes bearing an
412 exacerbated glycolytic status likely tied to prolonged and or excessive stimulation of
413 membrane bound TLRs in circulation, which results in DCs with an exhausted glycolytic
414 capacity. Although DCs stimulated with iMtb in the presence of a HIF-1α inhibitor
415 exhibited differences in activation markers and cytokine profile, we found that they were
416 still able to activate $CD4^+$ T cells from PPD+ donors in response to iMtb. These findings
417 complement previous evidence showing that LPS-induced mature DCs inhibit T-cell
418 responses through HIF-1α activation in the presence of glucose, leading to greater T cell
419 activation capacity in low glucose contexts such as at the interface between DCs and T
420 cells[25]. In this work, we did not detect an impact on T cell activation upon HIF-1α inhibition
421 in DCs, but we observed a clear reduction in their migration capacity that may limit or
422 delay DC encounters with T cells *in vivo*, leading to poor T cell activation in the lymph

423 nodes. In this regard, mouse studies have shown that DC migration directly correlates
424 with T cell proliferation[62]. However, we cannot rule out the possibility that other $CD4^+$ T
425 cell subsets (such as regulatory T cells), CD1-restricted T cells, and/or $CD8^+$ T cell
426 subsets could be differentially activated by iMtb-stimulated DCs lacking HIF-1α activity.
427
428 Three different populations of human monocytes have been identified: classical ($CD14^+$,
429 $CD16^-$), intermediate ($CD14^+$, $CD16^+$), and non-classical ($CD14^{dim}$, $CD16^+$) monocytes[63].
430 These monocyte subsets are phenotypically and functionally distinct. Classical
431 monocytes readily extravasate into tissues in response to inflammation, where they can
432 differentiate into macrophage-like or DC-like cells[64]; intermediate monocytes are well-
433 suited for antigen presentation, cytokine secretion, and differentiation; and non-classical
434 monocytes are involved in complement and Fc gamma-mediated phagocytosis and their
435 main function is cell adhesion[65,66]. Unlike non-classical monocytes, the two $CD14^+$
436 monocyte populations are known to extravasate into tissues and thus are likely to act as
437 precursors capable of giving rise to Mo-DCs in inflamed tissues. However, the DC
438 differentiation capacity of the intermediate population is still not well defined. We
439 previously demonstrated that monocytes from TB patients generate aberrant DCs, and
440 that $CD16^+$ monocytes generate aberrant DCs upon treatment with GM-CSF and IL-4[41].
441 Here, we demonstrated that glycolysis seems to play a dual role during DC differentiation
442 from monocytes, on the one side, being required for fully differentiated-DC migration to
443 lymph nodes in response to Mtb and, on the other side, leading to DCs with poor iMtb-
444 responsive migratory capacity if activated during the onset of DC differentiation. In this
445 regard, DCs from healthy subjects respond to iMtb by inducing a glycolytic and migratory
446 profile, while monocytes isolated from TB patients exhibit an unusual early glycolytic
447 state that results in the ulterior generation of DCs with low glycolytic and migratory
448 activities in response to Mtb. Similarly, we found that $CD16^+$ cells from TB patients
449 display an activated glycolytic status, as well as elevated HIF-1α expression levels

450 compared to their healthy counterparts. Additionally, we showed that monocytes from
451 TB patients are not only enriched in CD16^{+} cells, but also display an altered chemokine
452 receptor expression profile[67], demonstrating that both phenotype and function of a given
453 monocyte subset may differ under pathological conditions. While it is difficult to
454 determine whether the heightened glycolytic profile of monocytes may limit their
455 differentiation into DCs *in vivo*, we provided evidence that an increase in HIF1α-mediated
456 glycolysis in precursors leads to the generation of cells with poor ability to migrate in
457 response to CCL21 *in vitro.* In line with this observation, a recent study revealed a
458 significant increase in the glycolytic capacity occurs during the first 24 h of monocyte
459 differentiation towards a tolerogenic DC phenotype, as induced by vitamin D3[26],
460 highlighting the detrimental role of an early activated inflammatory profile in DC
461 precursors. A possible explanation for these effects may be found in lactate
462 accumulation in monocytes during DC differentiation. Lactate signaling in immune cells
463 leads to metabolic alterations in DCs that program them to a regulatory state[68], and
464 lactate has also been shown to suppress DC differentiation and maturation[18]; thus,
465 excessive precursor glycolytic activity may result in DCs biased toward regulatory
466 functions.
467
468 Taken together, our data offer new insights into the immunometabolic pathways involved
469 in the trafficking of DCs to the lymph nodes. These insights may have various
470 implications depending on factors such as timing, cell type, and location induction of the
471 HIF1α/glycolysis axis. On the one hand, nurturing HIF-1α-mediated glycolytic activity in
472 DCs during the early stages of infection could potentially enhance the effectiveness of
473 preventive strategies for TB. Particularly noteworthy is the significant impact revealed in
474 studies where the number of DCs reaching the lymph node proved to be a crucial factor
475 in determining the success of DC-based vaccination[62]. On the other hand, premature
476 activation of glycolysis in precursors, as observed in CD16+ monocytes from severe TB

patients, could disrupt the delicate balance necessary for an optimal immune response. This variability is consistent with the paradigm of "too much, too little," as demonstrated by the dual roles of IFNγ[69] and TNFα[70] in the context of TB. It also underscores the vital importance of maintaining an equilibrium in inflammatory responses. This study lays the foundation for further exploration into the potential systemic impact of the HIF1α/glycolysis axis within the realm of chronic inflammation contrasting with its role in a local setting during the acute phase of infection. By enhancing our understanding, these findings aim to guide the development of innovative preventive and therapeutic strategies for TB.

486 **Methods**

487 **Chemical Reagents**

488 LPS from Escherichia coli O111:B4 was obtained from Sigma-Aldrich (St. Louis, MO,
489 USA). Dexamethasone (Dx) was from Sidus (Buenos Aires, Argentina). PX-478 2HCL
490 was purchased from Selleck Chemicals (Houston, USA) and DMOG from Santa Cruz,
491 Biotechnology (Palo Alto, CA, USA). Additionally, GSK2837808A was purchased from
492 Cayman Chemical (Michigan, USA) together with echinomycin and sodium oxamate.

493

494 **Bacterial strain and antigens**

495 Mtb H37Rv strain was grown at 37°C in Middlebrook 7H9 medium supplemented with
496 10 % albumin-dextrose-catalase (both from Becton Dickinson, New Jersey, USA) and
497 0.05 % Tween-80 (Sigma-Aldrich). The Mtb γ-irradiated H37Rv strain (NR-49098) was
498 obtained from BEI Resource (NIAID, NIH, USA). The RFP-expressing Mtb strain was
499 gently provided by Dr. Fabiana Bigi (INTA, Castelar, Argentina).

500

501 **Preparation of monocyte-derived DCs**

502 Buffy coats from healthy donors were prepared at Centro Regional de Hemoterapia
503 Garrahan (Buenos Aires, Argentina) according to institutional guidelines (resolution
504 number CEIANM-664/07). Informed consent was obtained from each donor before blood
505 collection. Monocytes were purified by centrifugation on a discontinuous Percoll gradient
506 (Amersham, Little Chalfont, UK) as previously described[71]. Then, monocytes were
507 allowed to adhere to 24-well plates at $5x10^5$ cells/well for 1 h at 37°C in warm RPMI-
508 1640 medium (ThermoFisher Scientific, Waltham, MA). The mean purity of adherent
509 monocytes was 85 % (range: 80-92 %). The medium was then supplemented to a final
510 concentration of 10 % Fetal Bovine Serum (FBS, Sigma-Aldrich), human recombinant
511 Granulocyte-Macrophage Colony-Stimulating Factor (10 ng/ml, GM-CSF, Peprotech,
512 New Jersey, USA) and IL-4 (20 ng/ml, Biolegend, San Diego, USA). Cells were allowed
513 to differentiate for 5-7 days (DC-SIGN$^+$ cells in the culture > 90 %).

514

515 **DC stimulation**

516 DCs were stimulated with either irradiated Mtb (iMtb) or viable Mtb at equivalent OD_{600}
517 doses for 24 h at 37 ºC. The cells were washed three times, and their phenotype and
518 functionality were evaluated together with survival of activated cells; cell number and
519 viability were determined by either trypan blue exclusion assays or MTT. Infections were
520 performed in the biosafety level 3 (BSL-3) laboratory at the Unidad Operativa Centro de
521 Contención Biológica (UOCCB), ANLIS-MALBRAN (Buenos Aires), according to the
522 biosafety institutional guidelines.

523

524 **DC treatments**

525 When indicated, neutralizing monoclonal antibodies (mAb), or their corresponding
526 isotype antibodies as mock controls, were added 30 min prior to DC stimulation to inhibit
527 TLR2 (309717, Biolegend) or TLR4 (312813, Biolegend). In addition, DCs were
528 incubated with PX-478 (20 μM) or Echinomycin (1 nM) with the purpose of inhibiting HIF-
529 1α activity, DMOG (50 μM) to stabilize HIF-1α, and oxamate (20 mM) or GSK2837808A
530 (20 μM) to inhibit LDH. DC stimulation with iMtb occurred 30 min after treatment without
531 drug washout.

532 In figure 6 and S6, dexamethasone-induced tolerogenic dendritic cells (Dx-DC) were
533 generated by incubating DCs with 0.1 μM of dexamethasone for 1 h. Thereafter, cells
534 were washed, and "complete medium" was added. Tolerogenic Dx-DCs were then
535 stimulated (or not) with iMtb in the presence or not of DMOG (50 μM).

536

537 **Determination of metabolite concentrations**

538 Lactate production and glucose concentrations in the culture medium was measured
539 using the spectrophotometric assays Lactate Kit and Glicemia Enzimática AA Kit both
540 from Wiener (Argentina), which are based on the oxidation of lactate or glucose,
541 respectively, and the subsequent production of hydrogen peroxide[72]. The consumption

542 of glucose was determined by assessing the reduction in glucose levels in culture
543 supernatants in comparison with RPMI 10 % FBS. The absorbance was read using a
544 Biochrom Asys UVM 340 Microplate Reader microplate reader and software.
545

546 **Quantitative RT-PCR**

547 Total RNA was extracted with Trizol reagent (Thermo Fisher Scientific) and cDNA was
548 reverse transcribed using the Moloney murine leukemia virus reverse transcriptase and
549 random hexamer oligonucleotides for priming (Life Technologies, CA, USA). The
550 expression of the genes *HIF-1α* and *LDH-A* was determined using the PCR SYBR Green
551 sequence detection system (Eurogentec, Seraing, Belgium) and the CFX Connect Real-
552 Time PCR Detection System (Bio-Rad, CA, USA). Gene transcript numbers were
553 standardized and adjusted relative to eukaryotic translation elongation factor 1 alpha 1
554 (*EeF1A1*) transcripts. Gene expression was quantified using the ΔΔCt method. Primers
555 used for RT-PCR were as follows: EeF1A1 Fwd: 5'- TCGGGCAAGTCCACCACTAC -3'
556 and Rev: 5'-CCAAGACCCAGGCATACTTGA-3'; HIF-1α Fwd: 5'-
557 ACTAGCCGAGGAAGAACTATGAA-3' and Rev: 5'-TACCCACACTGAGGTTGGTTA-3';
558 and LDH-A Fwd: 5'-TGGGAGTTCACCCATTAAGC-3' and Rev: 5'-
559 AGCACTCTCAACCACCTGCT-3'.

560

561 **Immunofluorescence analysis**

562 FITC-, PE- or PerCP.Cy5.5-labelled mAbs were used for phenotypic analysis of the
563 following cell-surface receptor repertoires: FITC-anti-CD1a (clone HI149, eBioscience),
564 PE-anti-DC-SIGN (clone 120507, RD System), PerCP.Cy5.5-anti-CD86 (clone 374216,
565 Biolegend), FITC-anti-CD83 (clone HB15e, eBioscience), PE-anti-PD-L1 (clone MIH1,
566 BD Pharmingen) and in parallel, with the corresponding isotype control antibody.
567 Approximately $5x10^5$ cells were seeded into tubes and washed once with PBS. Cells
568 were stained for 30 min at 4ºC and washed twice. Additionally, cells were stained for 40

569 min at 4°C with fluorophore-conjugated antibodies PE-anti-Glut1 (clone 202915 R&D
570 Systems, Minnesota, USA) and in parallel, with the corresponding isotype control
571 antibody. For HIF-1α determination, DCs were permeabilized with methanol and
572 incubated with PE-anti-HIF-1α (clone 546-16, Biolegend). Stained populations were
573 gated according to forward scatter (FSC) and side scatter (SSC) analyzed on FACScan
574 (Becton Dickinson). Isotype matched controls were used to determine auto-fluorescence
575 and non-specific staining. Analysis was performed using the FCS Express (De Novo
576 Software) and results were expressed as median fluorescence intensity (MFI) or
577 percentage of positive cells.
578

579 **Soluble cytokines determinations**

580 Supernatants from DC populations or DC-T cell cocultures were harvested and
581 assessment of TNF-α, IL-10, IL-17A or IFN-γ production was measured by ELISA,
582 according to manufacturers' instructions (eBioscience). The detection limit was 3 pg/ml
583 for TNF-α and IL-17A, 6 pg/ml for IFN-γ, and 8 pg/ml for IL-10.
584

585 **$CD4^+$ T cell activation assay**

586 Specific lymphocyte activation (recall) assays were carried out in cells from tuberculin
587 purified protein derivative-positive skin test (PPD^+) healthy donors by culturing DC
588 populations and autologous T cells at a ratio of 10 T cells to 1 DC in round bottom 96-
589 well culture plates for 5 days as detailed previously[9]. The numbers of DCs were adjusted
590 to live cells before the start of the co-cultures. After 5 days, $CD4^+$ T cell subsets were
591 identified by immunolabeling according to the differential expression of CCR4, CXCR3,
592 and CCR6 as previously reported[73]: $CXCR3^+CCR4^-CCR6^-$ (Th1),
593 $CXCR3^-CCR4^+CCR6^-$ (Th2), $CXCR3^-CCR4^+CCR6^+$ (Th17), and $CXCR3^+CCR4^-CCR6^+$
594 (Th1* or Th1/Th17). The fluorochrome-conjugated antibodies used for flow cytometry
595 analysis were CD4-FITC (clone A161A1, Biolegend), CXCR3-PE-Cy7 (clone G025H7,

596 Biolegend), CCR4-PerCPCy5.5 (clone 1G1, BD Bioscience), CCR6-APC (clone 11A9,
597 BD Bioscience), and CD3-APC-Cy7 (clone HIT3a, Biolegend). A viability dye, Zombie
598 Violet (Biolegend), was used to exclude dead cells. Fluorescence Minus One (FMO)
599 control was used to set proper gating for CXCR3-PE-Cy7, CCR4-PerCPCy5.5, and
600 CCR6-APC detection. Cells were analyzed by fluorescence-activated cell sorting
601 (FACS), using the BD FACSCANTO cytometer and FlowJo™ Software (BD Life
602 Sciences).
603

604 **Chemotactic activity of DCs**

605 Each DC population ($4x10^5$ cells in 75 µl) was placed on the upper chamber of a transwell
606 insert (5 µm pore size, 96-well plate; Corning), and 230 µL of media (RPMI with 0.5 %
607 FCS) with human recombinant CCL21 (200 ng/ml) (Peprotech) was placed in the lower
608 chamber. After 3 h, cells that had migrated to the lower chamber were removed and
609 analyzed. The relative number of cells migrating was determined on a flow cytometer
610 using Calibrite beads (BD Biosciences), where a fixed number of beads was included in
611 each sample and the number of cells per 1,000 beads was evaluated. Data were
612 normalized to the number of initial cells.
613

614 ***In vivo* migration assay**

615 DCs were differentiated from bone marrow precursors obtained from naive BALB/c mice
616 in the presence of murine GM-CSF (10 ng/ml) and IL-4 (10 ng/ml) both from Biolegend
617 for 7 days. After differentiation, DCs were treated with oxamate (20 mM) or PX-478 (10
618 uM) and stimulated with iMtb. After 24 h, DCs were stained with CFSE (5 µM) and
619 inoculated intradermally in the inguinal zone of naïve BALB/c mice. 3 h post-injection,
620 inguinal lymph nodes close to the site of inoculation were harvested and cells were
621 stained with fluorophore-conjugated antibody PE-anti-CD11c (clone HL3, BD
622 Pharmingen). Analysis was performed using the FlowJo Software and results were
623 expressed as the percentage of $CFSE^+/CD11c^+$ cells.

624

625 **3D migration assay**

626 $0.5x10^5$ DCs were seeded on top of fibrillar collagen matrices polymerized from Nutragen
627 2 mg/ml, 10 % v/v MEM 10X (MEM invitrogen, Carlsbad, CA), UltraPure distilled water
628 and 4-6 % v/v bicarbonate buffer (pH=9) 7.5 %. After 24 h, cellular migration was
629 quantified by taking images using an inverted microscope (Leica DMIRB, Leica
630 Microsystems, Deerfield, IL) and the software Metamorph, as described previously[74].
631 Alternatively, in a similar manner, matrices were polymerized using Collagen (Sigma-
632 Aldrich, C9791-10MG) in figure 5C and D. After 24 h of cellular migration, matrices were
633 fixed with paraformaldehyde (PFA) 4 % during 30 min at room temperature and stained
634 with DAPI (Cell signaling). Collagen was removed and membranes were mounted with
635 DAKO. Images were taken by confocal microscopy (FluoView FV 1000), and cells were
636 counted per field.

637

638 **Measurement of cell respiration with Seahorse flux analyzer**

639 Bioenergetics were determined using a seahorse XFe24 analyzer. ATP production rates
640 and relative contribution from the glycolysis and the OXPHOS were measured by the
641 Seahorse XF Real-Time ATP Rate Assay kit. DCs ($2x10^5$ cells/well) were cultured in 3
642 wells per condition. The assay was performed in XF Assay Modified DMEM. Three
643 consecutive measurements were performed under basal conditions and after the
644 sequential addition of oligomycin and rotenone/antimycin (Agilent, USA). Extracellular
645 acidification rate (ECAR) and oxygen consumption rate (OCR) were measured.
646 Mitochondrial ATP production rate was determined by the decrease in the OCR after
647 oligomycin addition. On the other hand, the complete inhibition of mitochondrial
648 respiration with rotenone plus antimycin A, allows accounting for mitochondrial-
649 associated acidification, and when combined with proton efflux rate (PER) data, allows
650 calculation of Glycolysis ATP production rate. All OCR and ECAR values were
651 normalized. Briefly, before the assay brightfield imaging was performed. Cellular area

652 per condition was calculated by ImageJ software and imported into Wave (Agilent) using
653 the normalization function.
654
655 **SCENITH™ assay**
656 SCENITH experiments were performed as previously described[32] using the SCENITH kit
657 containing all reagents and anti-puromycin antibodies (www.scenith.com). Briefly, DCs
658 or PBMCs were treated for 40 min at 37°C in the presence of the indicated inhibitors of
659 various metabolic pathways and puromycin. After the incubation, puromycin was stained
660 using a fluorescently-labeled anti-Puromycin monoclonal antibody (clone R4743L-E8)
661 with Alexa Fluor 647 or Alexa Fluor 488, and analyzed by flow cytometry. For metabolic
662 analysis of monocyte subsets, PBMCs were labeled with PE-anti-CD16 (clone 3G8,
663 Biolegend) and PECy7-anti-CD14 (clone HCD14, Biolegend) mAbs. The impact of the
664 various metabolic inhibitors was quantitated as described[32].
665
666 **Transmission electron microscopy**
667 DCs were fixed in 2.5 % glutaraldehyde / 2 % PFA (EMS, Delta-Microscopies) dissolved
668 in 0.1 M Sorensen buffer (pH 7.2) for 1 h at room temperature, and then preserved in 1
669 % PFA dissolved in Sorensen buffer. Adherent cells were treated for 1 h with 1 %
670 aqueous uranyl acetate then dehydrated in a graded ethanol series and embedded in
671 Epon. Sections were cut on a Leica Ultracut microtome and ultrathin sections were
672 mounted on 200 mesh onto Formvar carbon coated copper grids. Finally, thin sections
673 were stained with 1 % uranyl acetate and lead citrate and examined with a transmission
674 electron microscope (Jeol JEM-1400) at 80 kV. Images were acquired using a digital
675 camera (Gatan Orius). For mitochondrial morphometric analysis, TEM images were
676 quantified with the ImageJ “analyze particles” plugin in thresholded images, with size
677 (μm^2) settings from 0.001 to infinite. For quantification, 8–10 cells of random fields (1000x
678 magnification) per condition were analyzed.

679

680 **Changes of mitochondrial mass**

681 Mitochondrial mass was determined in DCs by fixing the cells with PFA 4% and labeling
682 them with the probe MitoSpy Green FM (Biolegend). Green fluorescence was analyzed
683 by flow cytometry (FACScan, BD Biosciences).

684

685 **GeneSet Enrichment Analysis of human monocytes**

686 BubbleMap analysis was performed with 1,000 geneset-based permutations, and with
687 "Signal2Noise" as a metric for ranking the genes. The results are displayed as a
688 BubbleMap, where each bubble is a GeneSet Enrichment Analysis (GSEA) result and
689 summarizes the information from the corresponding enrichment plot. The color of the
690 Bubble corresponds to the population from the pairwise comparison in which the geneset
691 is enriched. The bubble area is proportional to the GSEA normalized enrichment score
692 (NES). The intensity of the color corresponds to the statistical significance of the
693 enrichment, derived by computing the multiple testing-adjusted permutation-based p-
694 value using the Benjamini–Yekutieli correction. Enrichments with a statistical
695 significance above 0.30 are represented by empty circles.

696

697 **Patient blood donors**

698 TB patients were diagnosed at the División Tisioneumonología, Hospital F.J.Muñiz
699 (Buenos Aires, Argentina) by the presence of recent clinical respiratory symptoms,
700 abnormal chest radiography, and positive culture of sputum or positive sputum smear
701 test for acid-fast-bacilli. Written, informed consent was obtained according to the Ethics
702 Committee from the Hospital Institutional Ethics Review Committee. Exclusion criteria
703 included HIV positive patients and the presence of concurrent infectious diseases or
704 comorbidities. Blood samples were collected during the first 15 days after
705 commencement of treatment. All tuberculous patients had pulmonary TB (Table I). The
706 term symptoms evolution refers to the time period during which a patient experiences

707 cough and phlegm for more than 2-3 weeks, with (or without) sputum that may (or not)
708 be bloody, accompanied by symptoms of constitutional illness (*e.g.,* loss of appetite,
709 weight loss, night sweats, and general malaise).
710

711 **Statistics**

712 All values are presented as the median ± SEM of 3-13 independent experiments. Each
713 independent experiment corresponds to 1 donor. For Seahorse assays, OCR and PER
714 values are shown as mean ± SD. Comparisons between unpaired experimental
715 conditions were made using either ANOVA for parametric data or Friedman test for non-
716 parametric data followed by Dunn's Multiple Comparison Test. Comparisons between
717 paired experimental conditions were made using the two-tailed Wilcoxon Signed Rank
718 Test for non-parametric data or T test for parametric data. Correlation analyses were
719 determined using the Spearman's rank test. A p-value of 0.05 was considered significant.
720

721 **Study approval**

722 *Human specimens.* The study design was reviewed and approved by the Ethics
723 Committees of the Academia Nacional de Medicina (49/20/CEIANM) and the Muñiz
724 Hospital, Buenos Aires, Argentina (NI #1346/21). All participants voluntarily enrolled in
725 the study by signing an informed consent form after receiving detailed information about
726 the research study.

727 *Mouse studies.* All experimental protocols were approved by the Institutional Animal
728 Care and Use of the Experimentation Animals Committee (CICUAL number 090/2021)
729 of the Institute of Experimental Medicine (IMEX, Buenos Aires).
730

AUTHOR CONTRIBUTIONS

Conceptualization & methodology: MM, FF, MFQ, MV, TPVM, CV and LB. Investigation: MM, MJ, ZV, JB, JLMF, MG, SM, MBV, FF, VGP, MV, CV and LB. Resources: SI, RM, LC, PGM, DP, RA, ON, CV, GL-V, MdCS and LB. Writing: MM, GL-V, RA, MdCS, ON, CV, TPVM and LB. Visualization: MM, FF, CV, TPVM and LB. Funding acquisition: ON, GL-V, RA, CV, and LB. Corresponding author: LB is responsible for ownership and responsibility that are inherent to aspects of this study.

ACKNOWLEDGMENTS

We thank the staff of the Regional Center of Hemotherapy of the Garrahan Hospital (Buenos Aires). We greatly thank Claire Lastrucci for designing the graphical abstract. In addition, we are grateful for the editing service provided by Life Science editors.

This work was supported by the Argentinean National Agency of Promotion of Science and Technology (PICT-2019-01044 and PICT-2020-00501 to LB); the Argentinean National Council of Scientific and Technical Investigations (CONICET, PIP 11220200100299CO to LB); the Centre National de la Recherche Scientifique, *Université Paul Sabatier*, the *Agence Nationale de Recherche sur le Sida et les hépatites virales (ANRS)* (ANRS2018-02, ECTZ 118551/118554, ECTZ 205320/305352, ANRS ECTZ103104 and ECTZ101971 to CV, ON and GL-V); and the French ANR JCJC-Epic-SCENITH ANR-20-CE14-0028 and CoPoC Inserm-transfert MAT-PI-17493-A-04 to RA. The funders had no role in study design, data collection, and analysis, decision to publish, or preparation of the manuscript.

References

1. Weiss, G. & Schaible, U. E. Macrophage defense mechanisms against intracellular bacteria. *Immunological Reviews* **264**, 182–203 (2015).

2. Khader, S. A. *et al.* Interleukin 12p40 is required for dendritic cell migration and T cell priming after Mycobacterium tuberculosis infection. *Journal of Experimental Medicine* (2006) doi:10.1084/jem.20052545.

3. Wolf, A. J. *et al.* Mycobacterium tuberculosis infects dendritic cells with high frequency and impairs their function in vivo. *Journal of immunology (Baltimore, Md. : 1950)* (2007) doi:10.4049/jimmunol.179.4.2509.

4. Cooper, A. M. Cell-Mediated Immune Responses in Tuberculosis. *https://doi.org/10.1146/annurev.immunol.021908.132703* **27**, 393–422 (2009).

5. Lai, R. *et al.* CD11b+ Dendritic Cell–Mediated Anti–Mycobacterium tuberculosis Th1 Activation Is Counterregulated by CD103+ Dendritic Cells via IL-10. *The Journal of Immunology* **200**, 1746–1760 (2018).

6. Urdahl, K. B., Shafiani, S. & Ernst, J. D. Initiation and regulation of T-cell responses in tuberculosis. *Mucosal immunology* **4**, 288–293 (2011).

7. Chandra, P., Grigsby, S. J. & Philips, J. A. Immune evasion and provocation by Mycobacterium tuberculosis. *Nature Reviews Microbiology 2022 20:12* **20**, 750–766 (2022).

8. Ernst, J. D. Mechanisms of M. tuberculosis Immune Evasion as Challenges to TB Vaccine Design. **24**, 34–42 (2018).

9. Balboa, L. *et al.* Monocyte-derived dendritic cells early exposed to Mycobacterium tuberculosis induce an enhanced T helper 17 response and transfer mycobacterial antigens. *International Journal of Medical Microbiology* **306**, 541–553 (2016).

10. Wolf, A. J. *et al.* Initiation of the adaptive immune response to Mycobacterium tuberculosis depends on antigen production in the local lymph node, not the lungs . *The Journal of Experimental Medicine* **205**, 105–115 (2008).

11. Balboa, L. *et al.* Mycobacterium tuberculosis impairs dendritic cell response by altering CD1b, DC-SIGN and MR profile. *Immunol Cell Biol* (2010) doi:10.1038/icb.2010.22.

12. Harding, C. V. & Boom, W. H. Regulation of antigen presentation by Mycobacterium tuberculosis: a role for Toll-like receptors. *Nat. Rev. Microbiol.* **8**, 296–307 (2010).

13. Srivastava, S., Grace, P. S. & Ernst, J. D. Antigen export reduces antigen presentation and limits T cell control of M. tuberculosis. *Cell Host Microbe* **19**, 44–54 (2016).

14. Roberts, L. L. & Robinson, C. M. Mycobacterium tuberculosis infection of human dendritic cells decreases integrin expression, adhesion and migration to chemokines. *Immunology* (2014) doi:10.1111/imm.12164.

15. Rajashree, P., Supriya, P. & Das, S. D. Differential migration of human monocyte-derived dendritic cells after infection with prevalent clinical strains of Mycobacterium tuberculosis. *Immunobiology* **213**, 567–575 (2008).

16. Currivan, E., Finlay, D. & Moreira, D. Dendritic cells metabolism: a strategic path to improve antitumoral DC vaccination. *Clinical and experimental immunology* **208**, 193–201 (2022).

17. Basit, F., Mathan, T., Sancho, D. & De Vries, J. M. Human dendritic cell subsets undergo distinct metabolic reprogramming for immune response. *Frontiers in Immunology* **9**, 2489 (2018).

18. Wculek, S. K., Khouili, S. C., Priego, E., Heras-Murillo, I. & Sancho, D. Metabolic Control of Dendritic Cell Functions: Digesting Information. **10**, 775 (2019).

19. Du, X., Chapman, N. M. & Chi, H. *Emerging Roles of Cellular Metabolism in Regulating Dendritic Cell Subsets and Function*. *Frontiers in Cell and Developmental Biology* vol. 6 (Frontiers Media SA, 2018).

20. Møller, S. H., Wang, L. & Ho, P. C. Metabolic programming in dendritic cells tailors immune responses and homeostasis. **19**, 370–383.

21. Everts, B. & Pearce, E. J. Metabolic control of dendritic cell activation and function: Recent advances and clinical implications. *Frontiers in Immunology* Preprint at https://doi.org/10.3389/fimmu.2014.00203 (2014).

22. Guak, H. *et al.* Glycolytic metabolism is essential for CCR7 oligomerization and dendritic cell migration. *Nat Commun* (2018) doi:10.1038/s41467-018-04804-6.

23. Liu, J. *et al.* CCR7 Chemokine Receptor-Inducible lnc-Dpf3 Restrains Dendritic Cell Migration by Inhibiting HIF-1α-Mediated Glycolysis. *Immunity* **50**, 600-615.e15 (2019).

24. Everts, B. *et al.* TLR-driven early glycolytic reprogramming via the kinases TBK1-IKKε supports the anabolic demands of dendritic cell activation. *Nat Immunol* **15**, 323 (2014).

25. Lawless, S. J. *et al.* Glucose represses dendritic cell-induced T cell responses. *Nature Communications* **8**, (2017).

26. Adamik, J. *et al.* Distinct metabolic states guide maturation of inflammatory and tolerogenic dendritic cells. *Nature Communications 2022 13:1* **13**, 1–19 (2022).

27. Kumar, R. *et al.* Immunometabolism of Phagocytes During Mycobacterium tuberculosis Infection. **6**, 105 (2019).

28. Marín Franco, J. L. *et al.* Host-Derived Lipids from Tuberculous Pleurisy Impair Macrophage Microbicidal-Associated Metabolic Activity. *Cell Rep* (2020) doi:10.1016/j.celrep.2020.108547.

29. Baay-Guzman, G. J. *et al.* Dual role of hypoxia-inducible factor 1 α in experimental pulmonary tuberculosis: Its implication as a new therapeutic target. *Future Microbiology* (2018) doi:10.2217/fmb-2017-0168.

30. Liu, J., Zhang, X., Cheng, Y. & Cao, X. Dendritic cell migration in inflammation and immunity. *Cell Mol Immunol* **18**, 2461–2471 (2021).

31. Freemerman, A. J. *et al.* Metabolic reprogramming of macrophages: glucose transporter 1 (GLUT1)-mediated glucose metabolism drives a proinflammatory phenotype. *The Journal of biological chemistry* **289**, 7884–7896 (2014).

32. Argüello, R. J. *et al.* SCENITH: A Flow Cytometry-Based Method to Functionally Profile Energy Metabolism with Single-Cell Resolution. *Cell Metab* (2020) doi:10.1016/j.cmet.2020.11.007.

33. Quesniaux, V. *et al.* Toll-like receptor pathways in the immune responses to mycobacteria. *Microbes and Infection* **6**, 946–959 (2004).

34. Chow, J. C., Young, D. W., Golenbock, D. T., Christ, W. J. & Gusovsky, F. Toll-like receptor-4 mediates lipopolysaccharide-induced signal transduction. *Journal of Biological Chemistry* **274**, 10689–10692 (1999).

35. Underhill, D. M., Ozinsky, A., Smith, K. D. & Aderem, A. Toll-like receptor-2 mediates mycobacteria-induced proinflammatory signaling in macrophages. *Proceedings of the National Academy of Sciences of the United States of America* **96**, 14459–14463 (1999).

36. Schwandner, R., Dziarski, R., Wesche, H., Rothe, M. & Kirschning, C. J. Peptidoglycan- and Lipoteichoic Acid-induced Cell Activation Is Mediated by Toll-like Receptor 2. *Journal of Biological Chemistry* **274**, 17406–17409 (1999).

37. Koh, M. Y. *et al.* Molecular mechanisms for the activity of PX-478, an antitumor inhibitor of the hypoxia-inducible factor-1α. *Molecular Cancer Therapeutics* **7**, 90–100 (2008).

38. Cairns, R. A., Papandreou, I., Sutphin, P. D. & Denko, N. C. Metabolic targeting of hypoxia and HIF1 in solid tumors can enhance cytotoxic chemotherapy. *Proceedings of the National Academy of Sciences of the United States of America* **104**, 9445–9450 (2007).

39. Kong, D. *et al.* Echinomycin, a Small-Molecule Inhibitor of Hypoxia-Inducible Factor-1 DNA-Binding Activity. *Cancer Research* **65**, 9047–9055 (2005).

40. Cougoule, C. *et al.* Podosomes, But Not the Maturation Status, Determine the Protease-Dependent 3D Migration in Human Dendritic Cells. *Frontiers in immunology* **9**, (2018).

41. Balboa, L. *et al.* Impaired dendritic cell differentiation of CD16-positive monocytes in tuberculosis: Role of p38 MAPK. *Eur J Immunol* (2013) doi:10.1002/eji.201242557.

42. Parlato, S. *et al.* Impaired IFN-α-mediated signal in dendritic cells differentiates active from latent tuberculosis. *PLOS ONE* **13**, e0189477 (2018).

43. Sakhno, L. V. *et al.* Impairments of Antigen-Presenting Cells in Pulmonary Tuberculosis. *Journal of immunology research* **2015**, (2015).

44. McGettrick, A. F. & O'Neill, L. A. J. The Role of HIF in Immunity and Inflammation. *Cell metabolism* **32**, 524–536 (2020).

45. Hillman, H. *et al.* Single-cell profiling reveals distinct subsets of CD14+ monocytes drive blood immune signatures of active tuberculosis. *Frontiers in Immunology* **13**, 1087010 (2023).

46. Spinelli, L., Carpentier, S., Montañana Sanchis, F., Dalod, M. & Vu Manh, T. P. BubbleGUM: Automatic extraction of phenotype molecular signatures and comprehensive visualization of multiple Gene Set Enrichment Analyses. *BMC Genomics* **16**, 1–11 (2015).

47. Reiley, W. W. *et al.* ESAT-6-specific CD4 T cell responses to aerosol Mycobacterium tuberculosis infection are initiated in the mediastinal lymph nodes. *Proceedings of the National Academy of Sciences* **105**, 10961–10966 (2008).

48. Griffiths, K. L. *et al.* Targeting dendritic cells to accelerate T-cell activation overcomes a bottleneck in tuberculosis vaccine efficacy. *Nat Commun* **7**, 1–13 (2016).

49. Harding, J. S., Rayasam, A., Schreiber, H. A., Fabry, Z. & Sandor, M. Mycobacterium-Infected Dendritic Cells Disseminate Granulomatous Inflammation. *Scientific Reports* **5**, (2015).

50. Samstein, M. *et al.* Essential yet limited role for CCR2+ inflammatory monocytes during Mycobacterium tuberculosis-specific T cell priming. *Elife* **2013**, (2013).

51. Semba, H. *et al.* HIF-1α-PDK1 axis-induced active glycolysis plays an essential role in macrophage migratory capacity. *Nature Communications* **7**, 1–10 (2016).

52. Kishore, M. *et al.* Regulatory T Cell Migration Is Dependent on Glucokinase-Mediated Glycolysis. *Immunity* **47**, 875-889.e10 (2017).

53. Park, J. S. *et al.* Mechanical regulation of glycolysis via cytoskeleton architecture. *Nature* **578**, 621–626 (2020).

54. Fernie, A. R., Zhang, Y. & Sampathkumar, A. Cytoskeleton Architecture Regulates Glycolysis Coupling Cellular Metabolism to Mechanical Cues. *Trends Biochem Sci* **45**, 637–638 (2020).

55. Ferreira, G. B. *et al.* Differential protein pathways in 1,25-dihydroxyvitamin d(3) and dexamethasone modulated tolerogenic human dendritic cells. *Journal of proteome research* **11**, 941–971 (2012).

56. Ferreira, G. B. *et al.* Proteome analysis demonstrates profound alterations in human dendritic cell nature by TX527, an analogue of vitamin D. *PROTEOMICS* **9**, 3752–3764 (2009).

57. Basit, F. & de Vries, I. J. M. Dendritic Cells Require PINK1-Mediated Phosphorylation of BCKDE1α to Promote Fatty Acid Oxidation for Immune Function. *Frontiers in Immunology* **10**, 2386 (2019).

58. Ohl, L. *et al.* CCR7 governs skin dendritic cell migration under inflammatory and steady-state conditions. *Immunity* **21**, 279–288 (2004).

59. Krawczyk, C. M. *et al.* Toll-like receptor-induced changes in glycolytic metabolism regulate dendritic cell activation. *Blood* **115**, 4742–4749 (2010).

60. Ryan, R. C. M., O'Sullivan, M. P. & Keane, J. Mycobacterium tuberculosis infection induces non-apoptotic cell death of human dendritic cells. *BMC Microbiol* **11**, 1–13 (2011).

61. Hackett, E. E. *et al.* Mycobacterium tuberculosis Limits Host Glycolysis and IL-1β by Restriction of PFK-M via MicroRNA-21. *Cell Reports* **30**, 124-136.e4 (2020).

62. Martín-Fontecha, A. *et al.* Regulation of Dendritic Cell Migration to the Draining Lymph Node Impact on T Lymphocyte Traffic and Priming. *Journal of Experimental Medicine* **198**, 615–621 (2003).

63. Ziegler-Heitbrock, L. *et al.* Nomenclature of monocytes and dendritic cells in blood. *Blood* **116**, e74–e80 (2010).

64. Ginhoux, F. & Jung, S. Monocytes and macrophages: developmental pathways and tissue homeostasis. *Nature Reviews Immunology* **14**, 392–404 (2014).

65. Wong, K. L. *et al.* Gene expression profiling reveals the defining features of the classical, intermediate, and nonclassical human monocyte subsets. *Blood* **118**, e16–e31 (2011).

66. Cros, J. *et al.* Human CD14dim monocytes patrol and sense nucleic acids and viruses via TLR7 and TLR8 receptors. *Immunity* **33**, 375–386 (2010).

67. Balboa, L. *et al.* Paradoxical role of CD16+CCR2+CCR5+ monocytes in tuberculosis: efficient APC in pleural effusion but also mark disease severity in blood. *J Leukoc Biol* (2011) doi:10.1189/jlb.1010577.

68. Manoharan, I., Prasad, P. D., Thangaraju, M. & Manicassamy, S. Lactate-Dependent Regulation of Immune Responses by Dendritic Cells and Macrophages. *Frontiers in Immunology* **12**, 691134–691134 (2021).

69. Kumar, P. IFNγ-producing CD4+ T lymphocytes: the double-edged swords in tuberculosis. *Clin Transl Med* **6**, 21 (2017).

70. Mootoo, A., Stylianou, E., Arias, M. A. & Reljic, R. TNF-α in tuberculosis: A cytokine with a split personality. *Inflamm Allergy Drug Targets* **8**, 53–62 (2009).

71. Genoula, M. *et al.* Formation of foamy macrophages by tuberculous pleural effusions is triggered by the interleukin-10/signal transducer and activator of transcription 3 axis through ACAT upregulation. *Front Immunol* (2018) doi:10.3389/fimmu.2018.00459.

72. Barham, D. & Trinder, P. An improved colour reagent for the determination of blood glucose by the oxidase system. *The Analyst* **97**, 142–5 (1972).

73. Acosta-Rodriguez, E. V. *et al.* Surface phenotype and antigenic specificity of human interleukin 17–producing T helper memory cells. *Nature Immunology 2007 8:6* **8**, 639–646 (2007).

74. Van Goethem, E., Poincloux, R., Gauffre, F., Maridonneau-Parini, I. & Le Cabec, V. Matrix architecture dictates three-dimensional migration modes of human macrophages: differential involvement of proteases and podosome-like structures. *Journal of immunology (Baltimore, Md. : 1950)* **184**, 1049–1061 (2010).

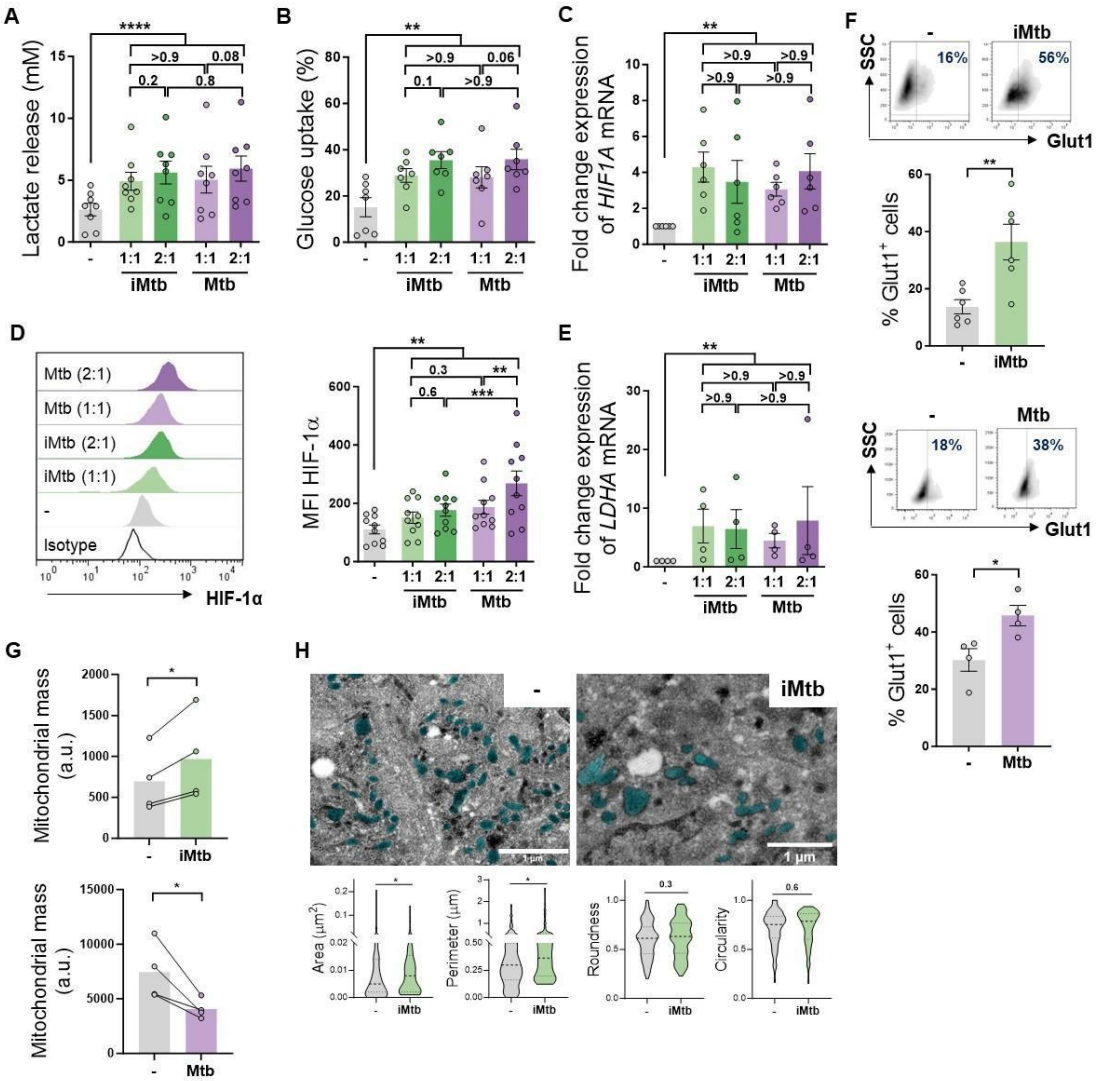

Figure 1. Mtb rewires the metabolic network of monocyte-derived DCs (Mo-DCs). Mo-DCs were stimulated with viable or irradiated Mtb (iMtb) at two MOI (1 or 2 Mtb per DC) for 24 h. Glycolysis was measured as: **(A)** Lactate release in culture supernatants (N=8); **(B)** Glucose uptake measured in culture supernatants (N=7); **(C)** Relative expression of *HIF-1α* mRNA normalized to *EeF1A1* control gene (N=6). **(D)** Representative histograms of the mean fluorescence intensity (MFI) of HIF-1α as measured by flow cytometry. Quantification shown in graph to the right (N=10). **(E)** Relative expression of lactate dehydrogenase A (*LDHA*) mRNA normalized to *EeF1A1* control gene (N=4). **(F)** FACS plots show the percentage of Glut1⁺ cells with and without iMtb stimulation or infected with viable Mtb in a representative experiment. Quantification of Glut1+ cells plotted below (N=4-6). **(G)** MFI of Mitospy probe as a measurement of mitochondrial mass for Mo-DCs treated (or not) with iMtb (upper panel) or infected with viable Mtb (lower panel). The data are represented as scatter plots with each circle representing a single individual, means ± SEM are shown (N=4). **(H)** Representative electron microscopy micrographs of control and iMtb-stimulated DCs showing mitochondria colored in cyan (left panels) and quantified morphometric analysis (right panels) (N=4). Statistical significance was assessed in **(A-E)** using 2-way ANOVA followed by Tukey's multiple comparisons test (∗p < 0.05; ∗∗p < 0.01; ∗∗∗∗p < 0.0001), and in **(F-H)** using paired t test (∗p < 0.05) for iMtb versus controls. All values are expressed as means ± SEM.

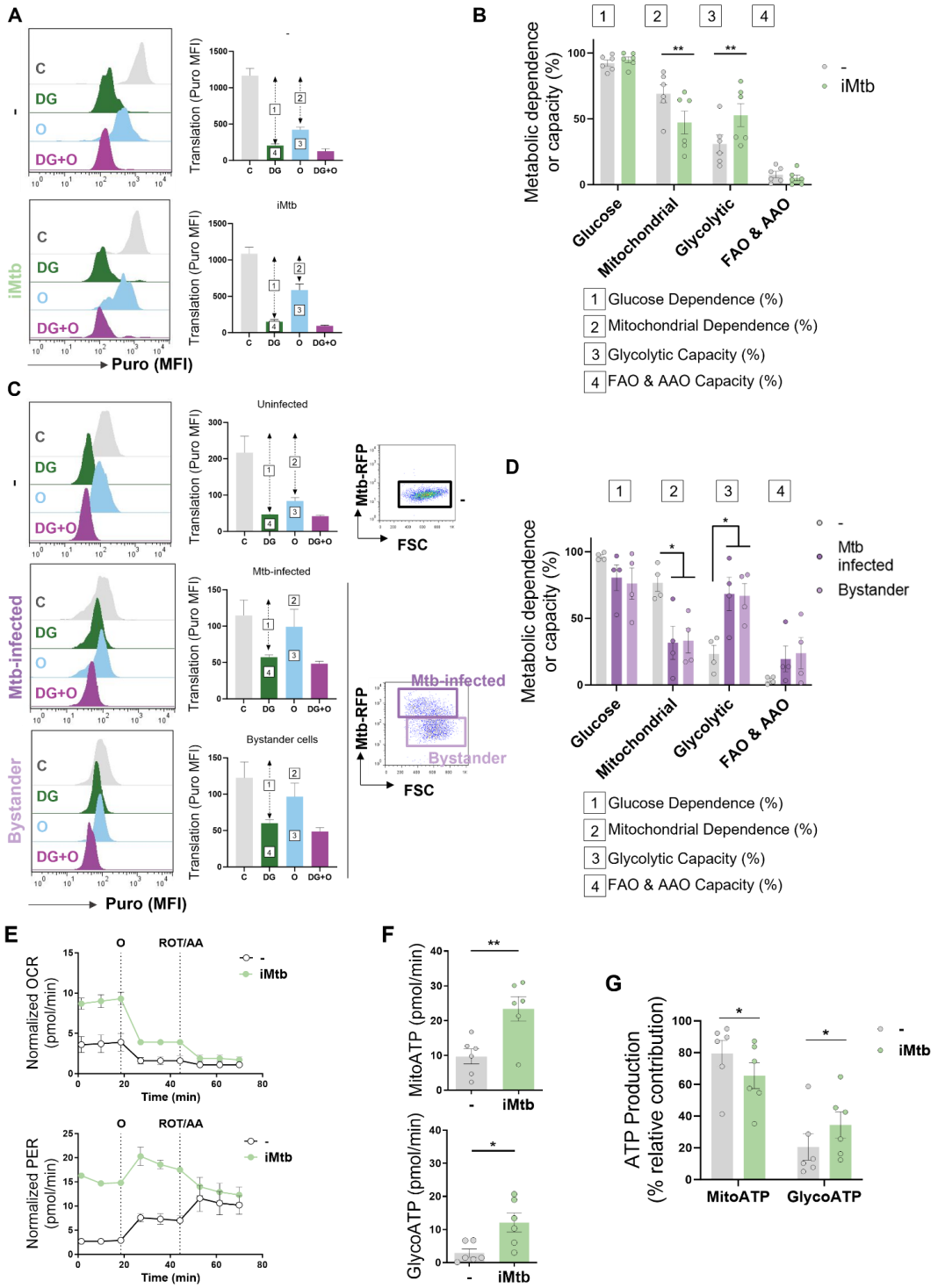

Figure 2. Mtb skews DC metabolism toward glycolysis. Mo-DCs were stimulated with irradiated Mtb (iMtb) or infected with Mtb expressing Red Fluorescent Protein (Mtb-RFP, panel C). **(A)** Representative histograms showing the translation level after puromycin (Puro) incorporation and staining with a monoclonal anti-Puro (anti-Puro MFI) in response to inhibitor treatment (C, Control; DG, 2-Deoxy-D-Glucose; Oligomycin, O; or combination treatment, DG+O). The bar plots show the values of the anti-Puro MFI from 6 donors. Arrows and numbers inside boxes denote the differences between the MFI of puro in the different treatments that are used to calculate the glucose dependence (1) and fatty acids and amino acids oxidation (FAO & AAO) capacity (4); and the mitochondrial dependency (2) and glycolytic capacity (3). **(B)** Relative contributions of glycolytic and FAO & AAO capacities and glucose and mitochondrial dependences to

overall DC metabolism analyzed with SCENITH (N=6)**. (C-D)** DCs were infected with Mtb-RFP for 24 h, thereafter the metabolic profile was evaluated by SCENITH. **(C)** Representative histograms showing the translation level after Puro incorporation are shown for uninfected, Mtb-infected and bystander DCs (those cells that are not infected directly but rather stand nearby). The bar plots show the values of the anti-Puro MFI from 4 donors. Right panel shows representative plots showing the gating strategy to distinguish the populations within Mtb-infected cultures, which includes RFP^+ (Mtb-infected DCs) and RFP^- (bystander DCs) cells. **(D)** Relative contributions of glycolytic and FAO & AAO capacities and glucose and mitochondrial dependences to DC metabolism (N=4). **(E)** Kinetic profile of proton efflux rate (PER; lower panel) and oxygen consumption rate (OCR; upper panel) measurements in control and iMtb-stimulated DCs in response to inhibitor treatments (Oligomycin, O; ROT/AA, Rotenone/Antimycin A), obtained using an Agilent Seahorse XFe24 Analyzer. PER and OCR measurements were normalized to the area covered by cells. **(F)** ATP production rate from mitochondrial oxidative phosphorylation (MitoATP) and glycolysis (glycoATP). MitoATP production rate and glycoATP production rate were calculated from OCR and ECAR measurements in control and iMtb-stimulated DCs (N=6). **(G)** Percentages of MitoATP and GlycoATP relative to overall ATP production (N=6). Statistics in **(B, F-G)** are from paired t test ($*p < 0.05$; $**p < 0.01$) for iMtb versus controls. Statistics in **(D)** are 2-way ANOVA followed by Tukey's multiple comparisons test ($*p < 0.05$) as depicted by lines. The data are represented as scatter plots with each circle representing a single individual, means ± SEM are shown.

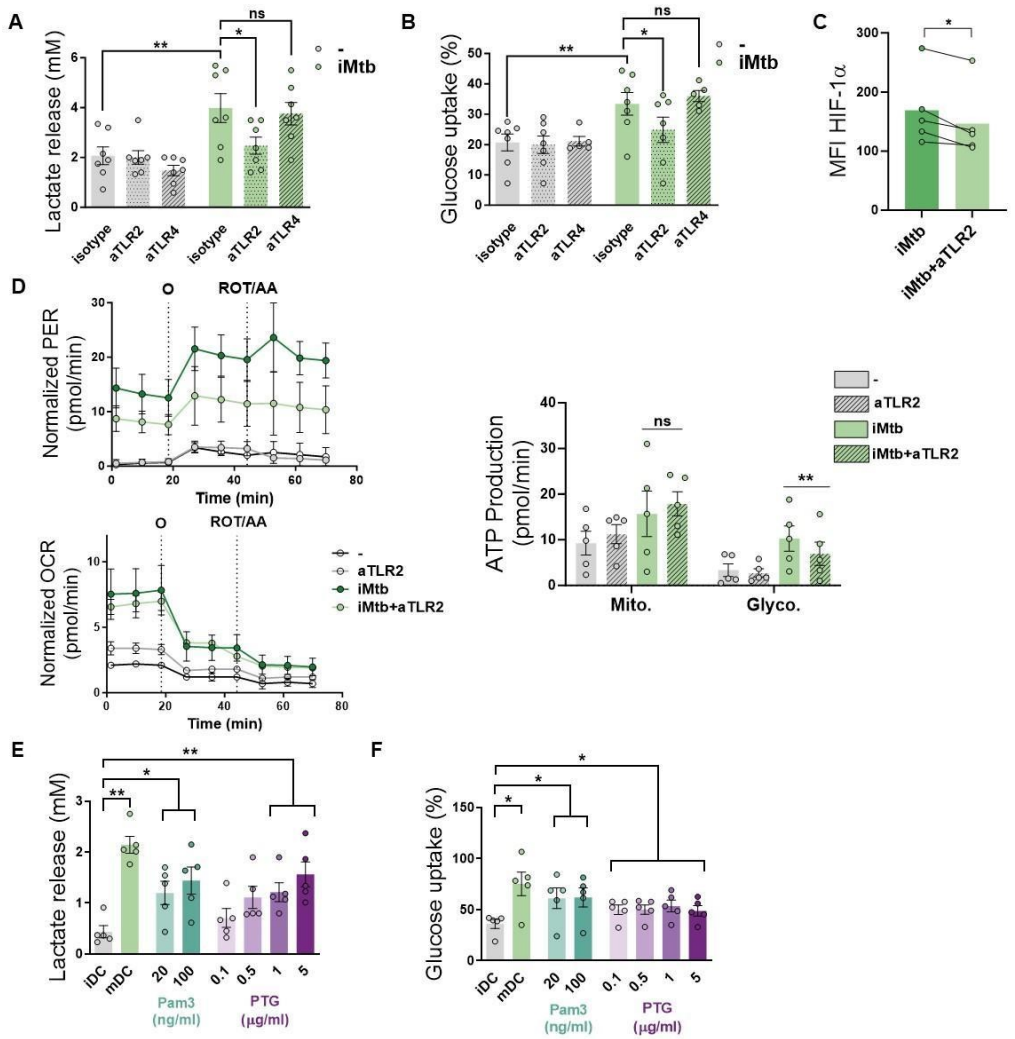

Figure 3. Mtb triggers glycolysis through TLR2 ligation in Mo- DCs. Mo-DCs were stimulated with irradiated Mtb (iMtb) in the presence of neutralizing antibodies against either TLR2 (aTLR2), TLR4 (aTLR4), or their respective isotype controls. **(A)** Lactate release as measured in supernatant (N=7). **(B)** Glucose uptake as measured in supernatant (N=7). **(C)** Mean fluorescence intensity (MFI) of HIF-1α as measured by flow cytometry (N=4). **(D)** Kinetic profile of proton efflux rate (PER) and oxygen consumption rate (OCR) measurements (left panels). Metabolic flux analysis showing quantification of mitochondrial ATP production and glycolytic ATP production (right panel) (N=5). **(E-F)** Mo-DCs were stimulated with Pam3Cys or Mtb peptidoglycan (PTG) at the indicated concentrations. **(E)** Lactate release as measured in supernatant (N=5). **(F)** Glucose uptake as measured in supernatant (N=5). Statistics in **(A-B, E-F)** are 2-way ANOVA followed by Tukey's multiple comparisons test (∗p < 0.05; ∗∗p < 0.01; ∗∗∗∗p < 0.0001). Statistics in **(C-D)** are from paired t test (∗p < 0.05) for iMtb versus controls. The data are represented as scatter plots with each circle representing a single individual, means ± SEM are shown.

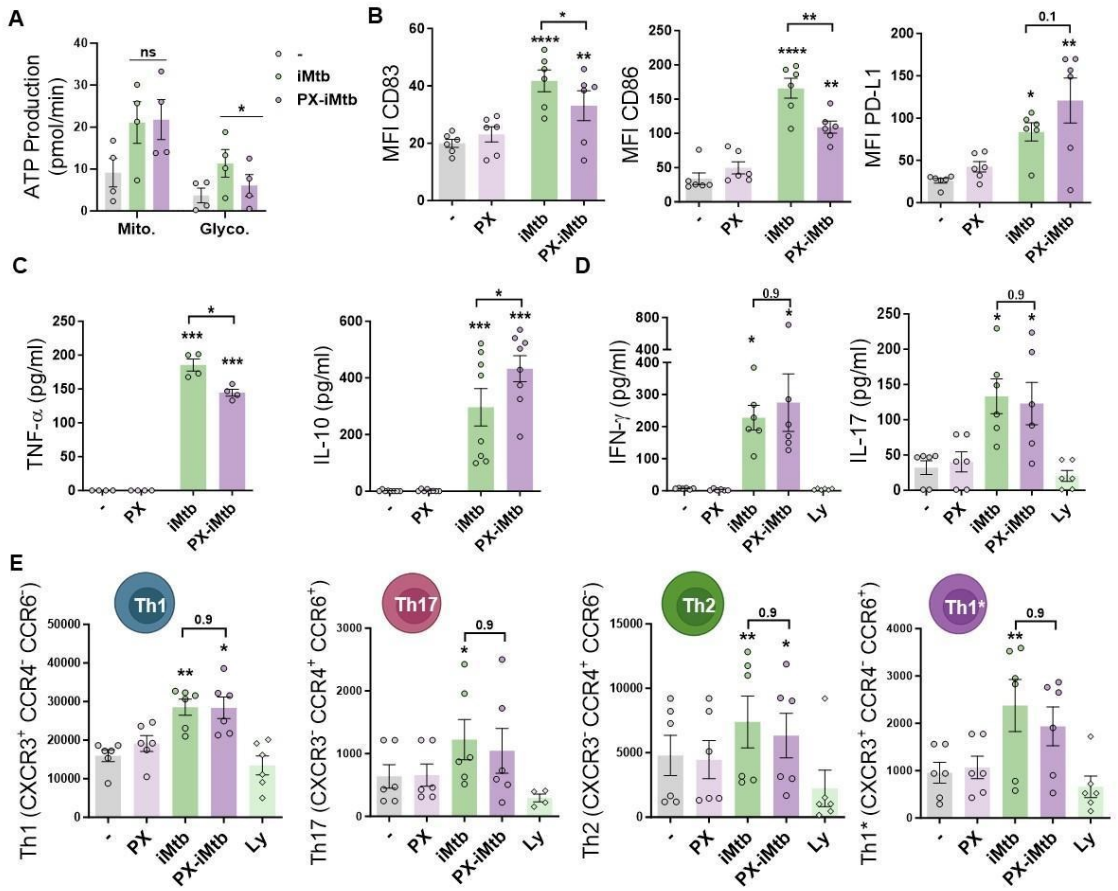

Figure 4. HIF-1α is required for DC maturation upon iMtb stimulation but not for CD4⁺ T lymphocyte polarization. (A-C) Mo-DCs were stimulated with irradiated Mtb (iMtb) in the presence or absence of the HIF-1α inhibitor PX-478 (PX). **(A)** Metabolic flux analysis showing quantification of mitochondrial ATP production and glycolytic ATP production, as in Figure 2C (N=4). **(B)** Mean fluorescence intensity (MFI) of CD83, CD86 and PD-L1 as measured by flow cytometry (N=6). **(C)** TNF-α and IL-10 production by Mo-DCs measured by ELISA (N=4-8). **(D-E)** Monocytes from PPD⁺ healthy donors were differentiated towards DCs, challenged or not with iMtb in the presence or absence of PX for 24 h, washed, and co-cultured with autologous CD4⁺ T cells for 5 days. **(D)** Extracellular secretion of IFN-γ and IL-17 as measured by ELISA (N=6). **(E)** Absolute abundance of Th1, Th17, Th2 and Th1/Th17 CD4⁺ T cells after coculture with DCs (N=6). When indicated lymphocytes without DCs were cultured (Ly). Statistical significance based on 2-way ANOVA followed by Tukey's multiple comparison test (∗p < 0.05; ∗∗p < 0.01). The data are represented as scatter plots with each circle representing a single individual, means ± SEM are shown.

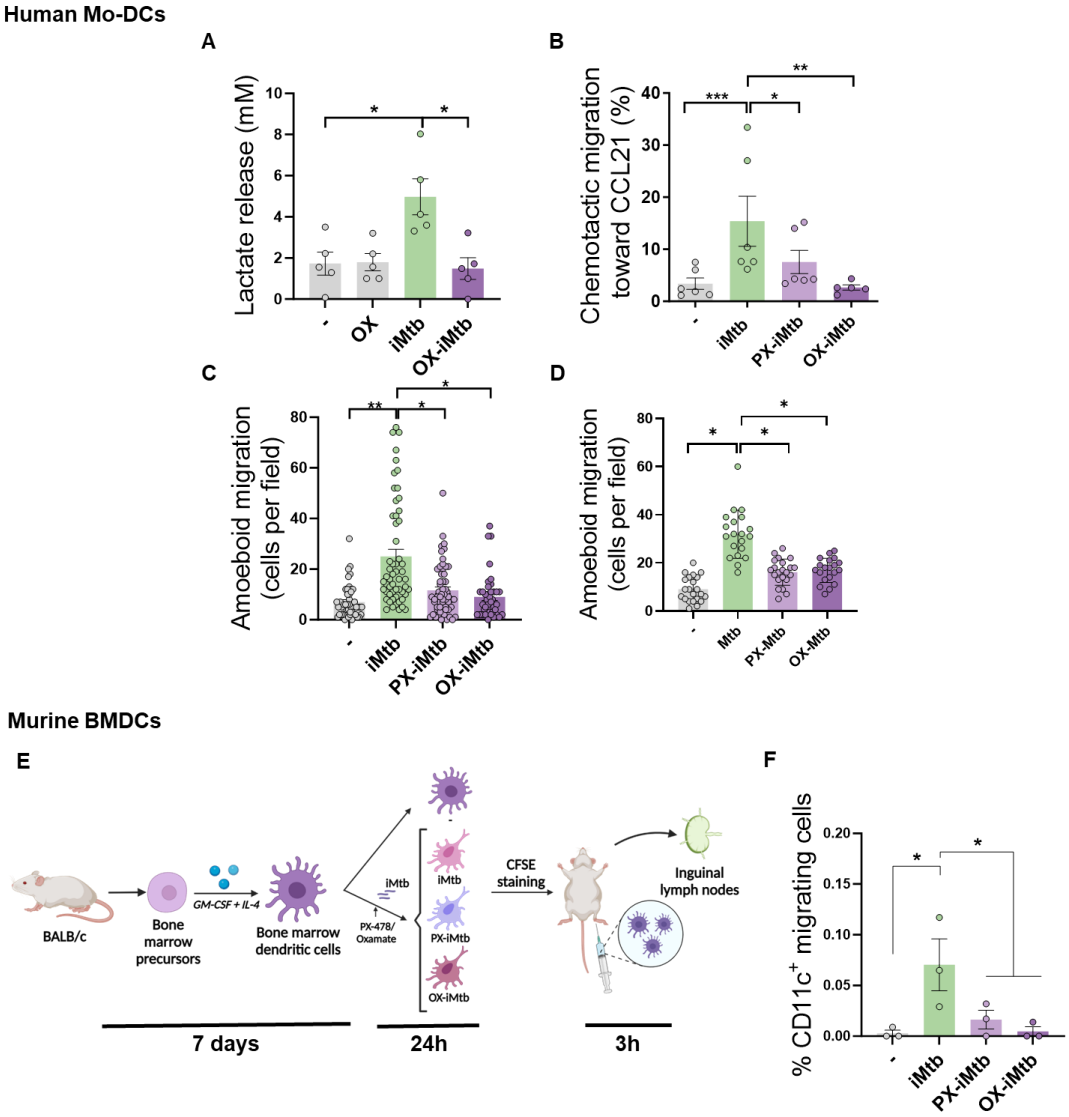

Figure 5. HIF1α-mediated-glycolysis is required to trigger migratory activity in iMtb-stimulated DCs. Mo-DCs were treated (or not) with HIF-1a inhibitor PX-478 (PX) or LDH inhibitor oxamate (OX) and stimulated with iMtb for 24 h. **(A)** Lactate release as measured in supernatants in DCs stimulated or not with iMtb in the presence of OX (N=5). **(B)** Percentage of migrated cells towards CCL21 relative to the number of initial cells per condition (N=6). **(C-D)** Three-dimensional amoeboid migration of DCs through a collagen matrix after 24 h. Cells within the matrix were fixed and stained with DAPI. Images of the membrane of each insert were taken and the percentage of cells per field were counted. **(C)** Mo-DCs stimulated with iMtb for 24 h (N=5). **(D)** Mo-DCs infected with Mtb for 24 h (N=4). The data are represented as scatter plots, where each circle represents a microphotograph sourced from either 5 (C) or 4 (D) independent donors, with each experiment typically including between five to ten microphotographs. **(E)** Representative schematic of the experimental setup for *in vivo* migration assays. **(F)** Percentages of migrating BMDCs (CFSE-labeled among $CD11c^+$) recovered from inguinal lymph nodes (N=3). Statistical significance assessed by **(A-B)** ANOVA followed by Dunnett's multiple comparisons test (∗p < 0.05; ∗∗p < 0.01); **(C-D)** Nested ANOVA followed by Dunnett's multiple comparisons test (∗p < 0.05; ∗∗p < 0.01); **(F)** ANOVA followed by Holm-Sidak's multiple comparisons test (∗p < 0.05).

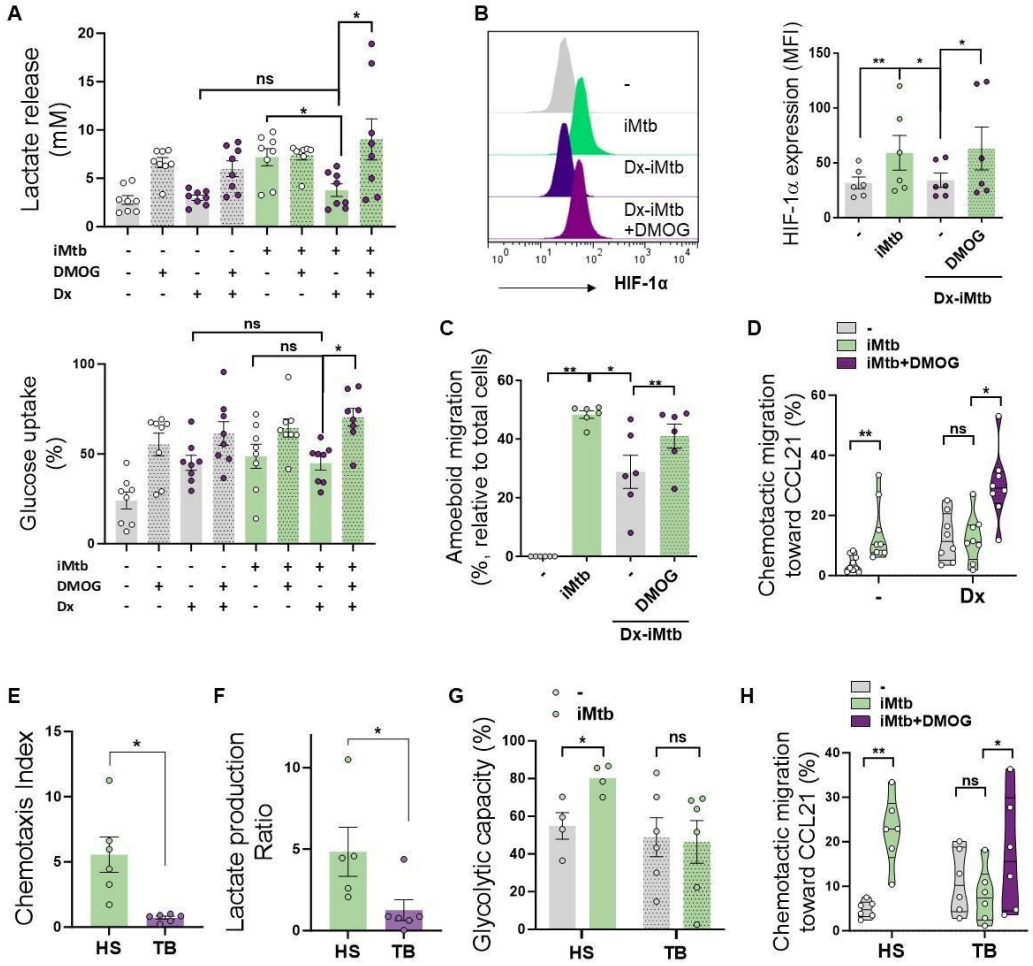

Figure 6. Stabilization of HIF-1α promotes migration of tolerogenic DCs and Mo-DCs from TB patients. Tolerogenic Mo-DCs were generated by dexamethasone (Dx) treatment and were stimulated (or not) with iMtb in the presence or absence of HIF-1α activator DMOG. **(A)** Lactate release and glucose uptake as measured in supernatant (N=8). **(B)** Mean fluorescence intensity (MFI) of HIF-1α. Representative histograms and quantification are shown (N=6). **(C)** Three-dimensional amoeboid migration of DCs through a collagen matrix. After 24 h of migration, images of stacks within the matrix were taken every 30 µm. Percentage of migrating cells were defined as cells in the stacks within the matrix relative to total number of cells (N=6). **(D)** Chemotactic activity towards CCL21 *in vitro* (N=6). **(E-H)** Mo-DCs were generated from healthy subjects (HS) or TB patients, and DCs were stimulated (or not) with iMtb. **(E)** Chemotaxis index towards CCL21 (relative to unstimulated DCs) (N=6). **(F)** Lactate production ratio relative to unstimulated DCs (N=6). **(G)** Glycolytic capacity assessed by SCENITH (N=4). **(H)** Chemotactic activity towards CCL21 of Mo-DCs from TB patients stimulated with iMtb and treated or not with DMOG (N=6). Statistical significance assessed by **(A-D)** 2-way ANOVA followed by Tukey's multiple comparisons test (∗p < 0.05; ∗∗p < 0.01); **(E-G)** Unpaired T test (∗p < 0.05); **(H)** Paired T test (∗p < 0.05). The data are represented as scatter plots with each circle representing a single individual, means ± SEM are shown.

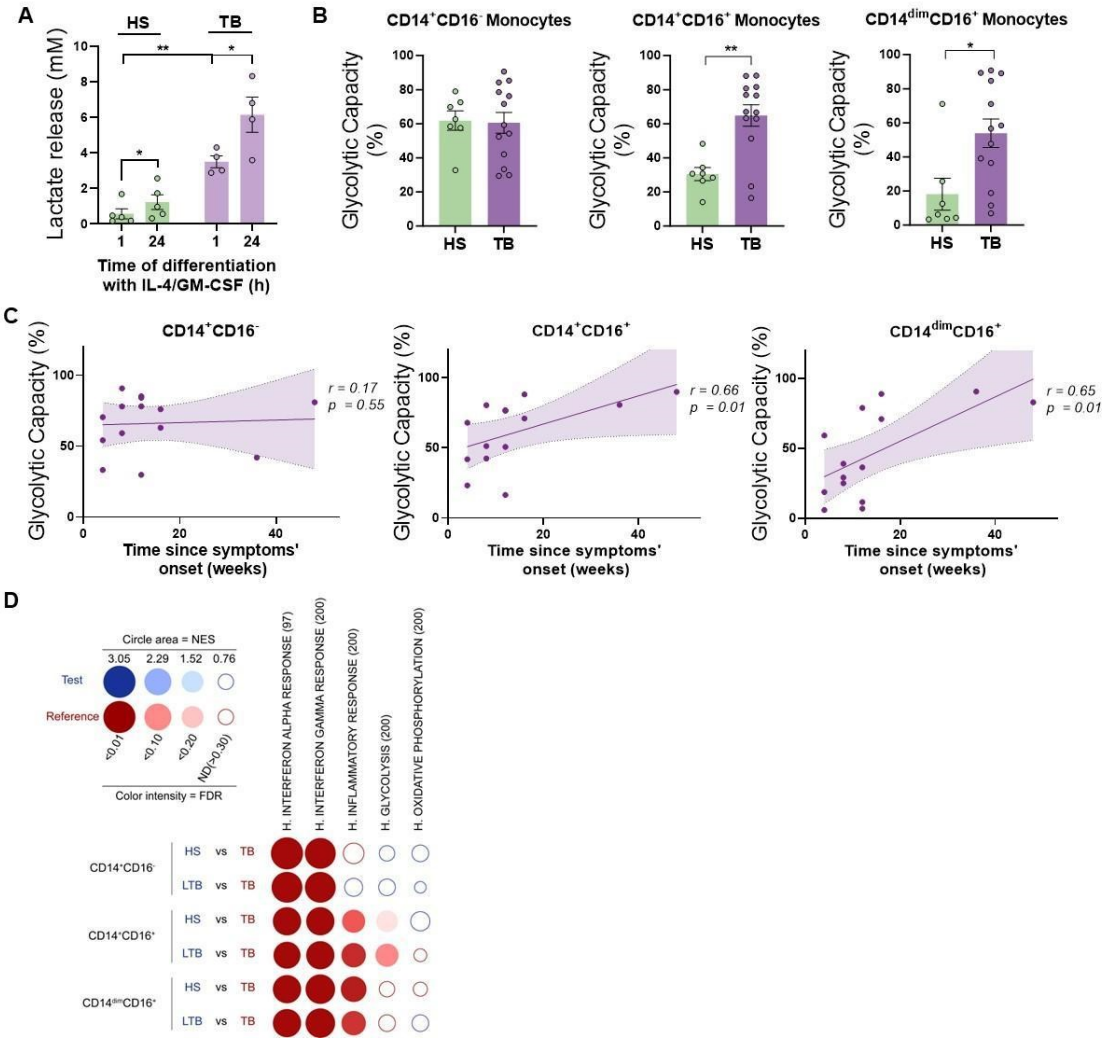

Figure 7. CD16⁺ monocytes from TB patients show increased glycolytic capacity. **(A)** Monocytes from TB patients or healthy subjects (HS) were isolated and cultured with IL-4 and GM-CSF for 24 h. Accumulation of lactate in culture supernatants were measured at 1 and 24 h of differentiation (N=5). (**B**) Glycolytic capacity measured by SCENITH of monocyte subsets as defined by their CD14 and CD16 expression from HS and TB patients (N=7). **(C)** Correlation analysis between the baseline glycolytic capacity and the evolution time of TB symptoms for each monocyte subset ($CD14^+CD16^-$, $CD14^+CD16^+$ and $CD14^{dim}CD16^+$, N=14). Linear regression lines are shown. Spearman's rank test. The data are represented as scatter plots with each circle representing a single individual, means ± SEM are shown. **(D)** BubbleMap analysis, a high-throughput extension of GSEA, on the pairwise comparisons of monocytes from healthy patients (HS) or donors with latent TB (LTB) vs patients with active TB (TB), for each monocyte subset ($CD14^+CD16^-$, $CD14^+CD16^+$ and $CD14^{dim}CD16^+$). The gene sets shown come from the Hallmark (H.) collection of the Molecular Signature Database (MSigDB). The colors of the BubbleMap correspond to the population from the pairwise comparison in which the geneset is enriched (red if geneset is enriched in TB). The bubble area is proportional to the GSEA normalized enrichment score (NES). The intensity of the color corresponds to the statistical significance of the enrichment, derived by computing the multiple testing-adjusted permutation-based p-value using the Benjamini–Yekutieli correction. Enrichments with a statistical significance above 0.30 are represented by empty circles. Statistical significance was assessed by **(A)** Paired T test for 0 *vs.* 24h ($*p < 0.05$) and 2-way ANOVA for HS *vs.* TB at each time ($**p < 0.01$); **(B)** unpaired T test ($*p < 0.05$; $**p < 0.01$).

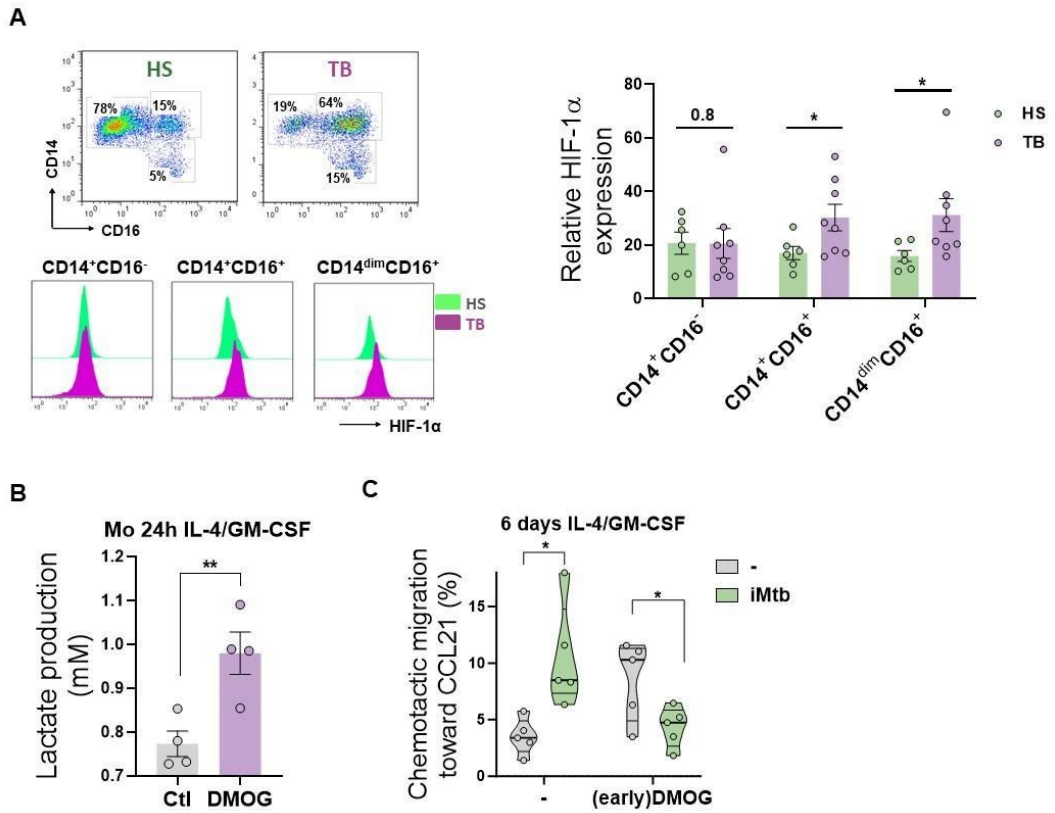

Figure 8. HIF1-α activation in CD16⁺ monocytes from TB patients leads to DCs with poor migration capacity. (A) *Ex-vivo* determination of HIF-1α expression by monocytes from healthy subjects (HS) or TB patients (TB) for each monocyte subset ($CD14^{+}CD16^{-}$, $CD14^{+}CD16^{+}$ and $CD14^{dim}CD16^{+}$) (N=6). **(B-C)** Monocytes from HS were treated with DMOG during the first 24 h of differentiation with IL-4/GM-CSF (earlyDMOG) and removed afterwards. On day 6 of differentiation, cells were stimulated (or not) with iMtb. **(B)** Monocyte lactate release after 24 h of DMOG addition (N=4). **(C)** Chemotactic activity towards CCL21 of DCs (N=5). Statistical significance was assessed by **(B)** paired T test (∗∗$p < 0.01$); **(C)** 2-way ANOVA followed by Tukey's multiple comparisons test (∗$p < 0.05$). The data are represented as scatter plots with each circle representing a single individual, means ± SEM are shown.

Table I. Demographic and clinical characteristics of TB patients

Age, years (range)	36 (19-67)
Gender, % (number/total)	M, 81% (31/38) F, 19% (7/38)
Nationality, % (number/total)	Argentina, 76.31% (29/38) Bolivia, 15.78% (6/38) Paraguay, 2.63% (1/38) Peru, 5.26% (2/38)
TB disease localization, % (number/total)	Pulmonary, 94% (36/38) Pulmonary + Extrapulmonary, 6% (2/38)
AFB* in sputum, % (number/total)	3+, 21% (8/38) 2+, 13% (5/38) 1+, 52% (20/38) -, 13% (5/38)
Leukocyte count, mean ± SEM, cell/µL	8483 ± 509
Lymphocyte mean ± SEM, %	19 ± 2
Monocyte mean ± SEM, %	7 ± 0,5

* Acid-fast-bacilli (AFB) in sputum: -, 1+, 2+, 3+ are defined according to the International Union Against Tuberculosis and Lung Disease (IUATLD)/ World Health Organization (WHO) quantification scale